Chapter 3
Instrumentation at Synchrotron Radiation Beamlines

Giuliana Aquilanti, Lisa Vaccari, Jasper Rikkert Plaisier and Andrea Goldoni

Abstract Today there are a number of third-generation synchrotron facilities around the world, which are dedicated to the production of extremely intense radiation, ranging from infrared to hard X-rays. The wavelength tunability and the very high brightness of these sources have opened a wide range of new characterization procedures for research purposes. This paragraph is intended to describe various facets of both technological and analytical methods using synchrotron radiation, in order to help researchers and students who are interested in the study of materials. First, a concise introduction to synchrotron facilities and an overview of the main characteristics of the existing third-generation sources are presented. Then a basic line-up of beamlines for different energy ranges as well as the problems associated to beamline constructions and choices are described. Finally, for each energy range, a brief description of some techniques available in third-generation synchrotron facilities is given.

3.1 Introduction

When synchrotrons were first developed, their primary purpose was to accelerate particles to study the atomic nucleus, and not specifically designed to generate light. Nowadays only a few of them still used as colliders for high-energy physics

G. Aquilanti · L. Vaccari · J. R. Plaisier · A. Goldoni (✉)
Elettra-Sincrotrone Trieste S.C.p.A, Strada Statale 14-km 163, AREA Science Park 5, 34149 Basovizza, Trieste, Italy
e-mail: Andrea.Goldoni@elettra.eu

G. Aquilanti
e-mail: giuliana.aquilanti@elettra.eu

L. Vaccari
e-mail: lisa.vaccari@elettra.eu

J. R. Plaisier
e-mail: jasper.plaisier@elettra.eu

S. Mobilio et al. (eds.), *Synchrotron Radiation*,
DOI: 10.1007/978-3-642-55315-8_3,

experiments such as the Large Hadron Collider at CERN, but there are many more synchrotrons dedicated to exploit the special characteristics of the generated light. From the early 1990s machines were designed with insertion devices from scratch. The first such third-generation source, the European Synchrotron Radiation Facility (ESRF) in Grenoble, France, started operating in 1994. Insertion devices (undulators and wigglers) are arrays of magnets placed into the straight sections of the storage ring. They help to create a very bright beam with intensity peaks with a wavelength that can be varied by adjusting the field strength (often the gap between two magnet arrays). The demand for synchrotron light led to the construction of 3rd-generation machines around the world and to constant upgrades of existing ones to provide brighter light, increased user hours and more flexible experimental stations. The modular nature of modern synchrotrons allows new technologies to be incorporated into existing machines. By using powerful linear accelerator technology, fourth-generation sources—known as free-electron lasers (FELs)—can generate shorter, femtosecond pulses with a peak intensity comparable to the one emitted by synchrotron sources in one second, therefore producing X-rays that are millions of times brighter in each pulse. FELs are complementary to third-generation machines, enabling studies requiring very high peak brightness.

There are now more than 50 dedicated light sources in the world, both of second- and third-generation. They cover a wide spectral (frequency) range from infrared to the hard X-rays. The emitted light is characterized by high brightness, many orders of magnitude brighter than conventional sources. The light is highly polarized, tunable, collimated (consisting of almost parallel rays). These machines support a huge range of applications, from condensed matter physics to structural biology, environmental science and cultural heritage.

As shown in Table 3.1 the majority of 3rd generation sources operate with electron beam in the medium-energy range (2–4 GeV). Only a few of 3rd generation synchrotrons are optimized to work in the high-energy range of electron beams (6–8 GeV) in order to produce high intensity X-rays in 10–50 keV range (ESRF, PETRA III, Spring8, APS). Since many X-ray diffraction studies are performed in the range up to 20 keV, the medium-energy machines may be competitive with the high-energy ones in many areas of science, against a fraction of their costs. On the other hand, at a photon energy of 10 keV, medium-energy sources typically have an order of magnitude smaller brilliance than, e.g., ESRF. In the soft X-ray range, however, they are of course superior in performance.

Nowadays, many 3rd generation synchrotrons operate in top-up mode. Small injections at relatively short intervals compensate for the loss of electron current. A constant current in the storage ring gives rise to a constant heat load on the ring chamber including the electron optical elements along its circumference. This in turn has been shown to lead to an exceptionally high position stability of the beam. A constant temperature in the ring tunnel within 0.1 °C and a stable mounting of the magnets of the ring lattice onto girders with a positioning accuracy of ca 30 mm are also essential for obtaining high level of stability. Important for beam stability and essential for top-up injection is the use of a full-energy injector. At the Elettra synchrotron, full-energy injection is achieved through the use of a booster that is

Table 3.1 Third generation sources in operation and under construction

Light sources	Energy (GeV)	Current (mA)	Emittance (μm rad)	Ring (m)	Linear sections	Web site www.
ESRF	6.0	200	4.0	844.4	32	www.esrf.eu
APS	7.0	100	3.0	1104	40	www.aps.anl.gov
SPring-8	8.0	100	3.4	1436	48	www.spring8.or.jp
ALS	1.9	400	6.3	196.8	12	www.als.lbl.gov
TLS	1.5	240	25	120	6	www.nsrrc.org.tw
Elettra	2–2.4	300–170	7.0	259	12	www.elettra.eu
PLS	2.5	200	12.0	280.6	12	www.paleng.postech.ac.kr
LNLS	1.37	250	100	93.2	6	www.lnls.cnpem.br
MAX-II	1.5	280	9.0	90	10	www.maxlab.lu.se
BESSY-II	1.7	200	6.1	240	16	www.helmholtz-berlin.de/zentrum/grossgeraete/elektronenspeicherring
Siberia-II	2.5	200	98	124	12	www.ssrc.inp.nsk.su
New SUBARU	1.5	500	38	119	6	www.lasti.u-hyogo.ac.jp
SLS	2.4	400	5	288	12	www.psi.ch/sls
ANKA	2.5	200	50	110.4	8	www.anka.kit.edu
CLS	2.9	300	22.7	171	12	www.lightsource.ca
SPEAR-3	3.0	500	18	234	18	www.ssrl.slac.stanford.edu/spear3
SAGA-LS	1.4	300	7.5	75.6	8	www.saga-ls.jp
SOLEIL	2.75	500	3.75	354	24	www.synchrotron-soleil.fr
Diamond	3.0	300	2.7	561.6	24	www.diamond.ac.uk
ASP	3.0	200	10	216	14	www.synchrotron.org.au

(continued)

Table 3.1 (Continued)

Light sources	Energy (GeV)	Current (mA)	Emittance (μm rad)	Ring (m)	Linear sections	Web site www.
Indus II	2.5	300	58.1	172.5	8	www.cat.ernet.in/technology/accel/indus
SSRF	3.5	300	3.9	432	20	www.ssrf.sinap.ac.cn
ALBA	3.0	400	4.3	269	24	www.cells.es
PETRA III	6.0	100	1.0	2304	20	www.petra3.desy.de
PLS-II	3.0	400	5.8	280	24	www.paleng.postech.ac.kr
TPS	3.0	400	1.7	518	24	www.nsrrc.org.tw
NSLS-II	3.0	500	1.5	792	30	www.bnl.gov/ps/nsls2
SESAME	2.5	400	26	133	16	www.sesame.org.jo
CANDLE	3.0	350	8.1	216	16	www.candle.am
MAX IV Two rings	1.5–3	500	5.6/0.24	96/528	12/20	www.maxlab.lu.se/maxiv

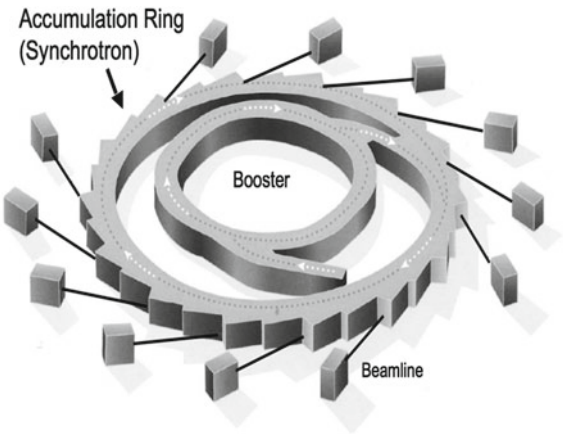

Fig. 3.1 General scheme of a 3rd generation synchrotron, with booster and beamlines tangent to the circumference

installed in the same tunnel of and concentric to the storage ring. The booster provides a low emittance, resulting in a good matching to the ring acceptance and hence a high injection efficiency in the top-up mode.

Considering the insertion devices, there is a trend toward the use of undulators instead of wigglers. Anyway, for certain techniques, like X-ray absorption spectroscopy, the use of sources with a large energy range emission may be preferred.

The experimental configurations of different synchrotron facilities are quite similar (see Fig. 3.1). The storage rings where the light is generated have many ports, each of them opening onto a beamline. Here scientists set up their experiments and collect data. Beamlines are built tangentially to the electron beam orbit of the storage ring and capture the radiation emitted from bending magnets, wigglers or undulators. The beamlines, however, have optical schemes that depend on the experimental methods they are used for.

It has to be highlighted that the precise missions of the beamlines are likely to evolve accordingly to their scientific goals and their capabilities will be continuously improved by the synergic interactions with the user community. The following pages offer a brief description of instruments available in different beamlines depending on the working energy and techniques. In general, standard beamline components that are addressed in this section consist of filters, slits, photon shutters, monochromators, and mirrors. Of these components, the monochromators and mirrors have the greatest importance, complexity, and cost, so more effort will be dedicated in describing these latter components.

3.2 Beamlines in the Hard X-Ray Range (2000–50000 eV)

A synchrotron beamline can be divided in two main parts: the optical section and the experimental station. In the next paragraphs the typical optical instrumentation for a beamline designed to work in the hard X-ray range will be discussed. We will

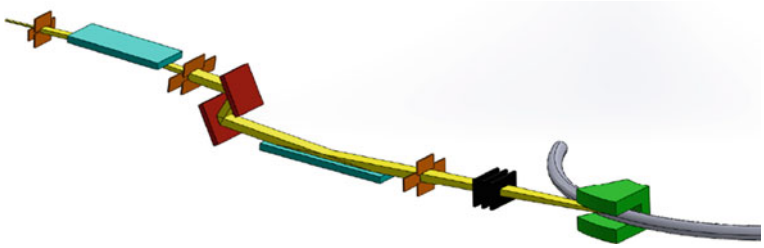

Fig. 3.2 Schematic overview of the optics of a typical beamline operating in the hard X-ray range

briefly show the most common systems to detect hard X-rays, and finally we will give the description of two beamlines operating at the Elettra synchrotron dedicated to X-ray diffraction and X-ray absorption spectroscopy respectively.

3.2.1 Hard X-Ray Optics

A typical optical scheme for a beamline working in the hard X-ray range is shown in Fig. 3.2.

Low absorbing windows (typically beryllium or polymeric windows) along a beamline are used to separate different vacuum sections. Very often a window is installed just after the front end to separate the beamline vacuum from the machine vacuum. Windows are also used to absorb a significant fraction of the unused low-energy radiation, therefore reducing the overall power delivered to the downstream components. The windows can be protected to prevent thermal failures and additional attenuator packages may be used to further manage the power load on the optical components. Filters and windows effectively establish the lower limit of the energy range of a beamline. Slits are also present along the beamline. These are used to define the size of the beam. They are set to accept the beam horizontally and vertically according to the specification of the optics. Slits are also used also to eliminate spurious beam scattered from the optics.

X-ray mirrors are used both as high-energy cut-off filters to remove unwanted higher order harmonics delivered by the monochromators and as focusing devices. In addition, they reduce the power load on the more delicate single crystal monochromators present along the beamline.

When used as high-energy cut-off, specular reflection must be taken into account. This is related to the index of refraction n, given in the X-ray regime, by Parrat [1]:

$$n = (1 - \delta) - i\beta$$

where the quantities δ and β are related to dispersive and absorptive nature of the materials. As the index of refraction is less than unity, X-rays incident on a material

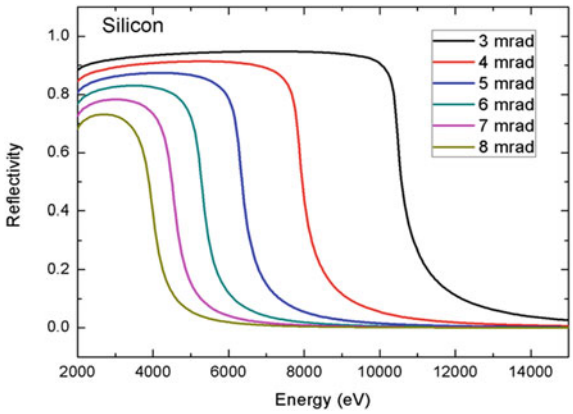

Fig. 3.3 Reflectivity of Silicon as a function of energy for different glancing angles

are totally reflected if the glancing angle θ is less than the critical angle θ_c. Otherwise, they are absorbed by the material. From Snell's law:

$$\theta_c = \sqrt{2\delta}$$

in the absence of absorption edges. θ_c, for usual mirror materials, is in the order of milliradiants, e.g. $\theta_c = 5.1$ mrad for α-quartz silica and $\theta_c = 10$ mrad for gold at $\lambda = 1.54$ Å. The mirror reflectivity ρ as a function of angle (or energy) is a step-like function, the step occurring at the critical angle (or energy). Figure 3.3 shows the reflectivity of Si (density: 2.33 mg/cm^3) at different glancing angles. Typical substrate materials are Si and/or SiO_2. Coating materials are Pt, Rh, Ni, Au depending on the energy, reflectivity and absorption edges.

Because of such small glancing angles, the X-ray mirrors may be connected to a feedback system with a beam position monitor close to the experiment. In this way small variations in the beam position can automatically be adjusted by repositioning the mirror.

The second application of X-ray mirrors is to collimate or to focus the beam onto the following optical element or the sample. The efficiency of collimation/focusing is determined by aberrations and by the mirror imperfections such as micro-roughness and slope errors. The best conditions are obtained with an elliptical or parabolic shape of the mirror surface although, very often, these shapes are approximated by spheres or cylinders. Mirrors can also be bent dynamically in meridional direction for adjusting the curvature when changing the glancing angle, for correcting deformation arising from gravitation and thermal load and to obtain a parallel, focused or divergent beam on the sample depending on the nature of the experiment. A dynamical sagittal focusing is also possible. Figure 3.4 shows a drawing of a toroidal mirror, which is curved in both meridional and sagittal directions.

When the mirror is used as the first optical element in the beamline, problems related to radiation damage and thermal gradients arise. These create strains, which

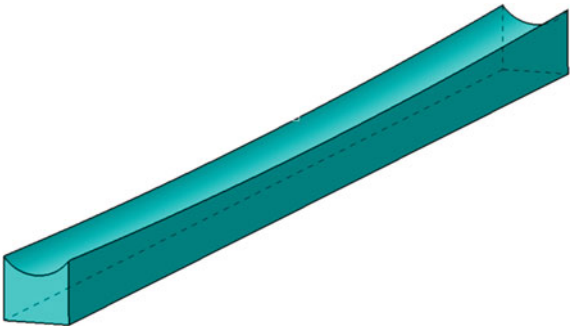

Fig. 3.4 Drawing of a toroidal X-ray mirror. Both meridional and sagittal curvatures are visible

deform the surface and degrade mirror performances. Nonetheless, the X-ray mirrors have the advantage that the heat and the radiation are spread over a large surface because the reflection angle is very small. Typical length for X-ray mirrors is 1 m with radius of curvature of the order of kilometers and centimeters in the meridional and sagittal directions respectively.

Contrary to laboratory X-ray sources, synchrotron sources as bending magnets and wigglers produce a broad spectrum of wavelengths. In the hard X-ray regime single crystal monochromators are employed to monochromatize the X-ray beam. The role of the monochromators is to deliver an X-ray beam with a high monochromaticity with an energy resolution $\Delta E/E \leq 10^{-4}$ for the most common applications and high intensity of reflection. In X-ray monochromators, diffraction from perfect crystals (typically silicon, germanium, diamond) is used to monochromatize the beam. The condition for X-ray diffraction is expressed by Bragg's law:

$$2d \sin \theta = n\lambda$$

where d is the spacing of crystal lattice planes, λ is the wavelength and θ is the incident angle. The integer n denotes the reflection order, and thus wavelengths λ, $\lambda/2$, $\lambda/3$, …, λ/n are diffracted simultaneously as far as the reflections are not forbidden by the crystal structure. For instance, in the case of Si, the structure factor of the second order reflection is zero, but the third-order reflection might be present. In practice, this means that when selecting, for instance a photon energy of 7 keV, photons with an energy of 21 keV will be present as well. Since $\sin \theta$ is less than one, a set of Bragg planes does not reflect wavelengths longer than $2d$. Therefore long wavelengths require large interplanar spacing. On the other hand, excessively large d spacing causes the Bragg angle to be inconveniently small, leading to degraded separation of the reflected beam from the scattered radiation. In the ideal case, the d spacing of the crystal of the monochromator must match the wavelength to be selected.

As mentioned above, an important property of a monochromator is the energy resolution. In the differential form of the Bragg equation

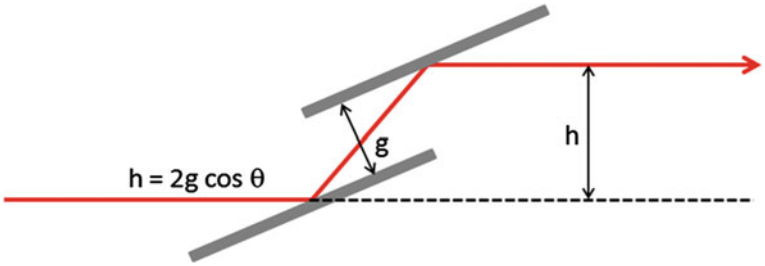

Fig. 3.5 Principle of a double crystal monochromator

$$\frac{\Delta E}{E} = \frac{\Delta\lambda}{\lambda} = \Delta\theta \cot\theta_B$$

the energy resolution is determined by the angular spread $\Delta\theta$ and the Bragg angle θ_B. In fact, within the dynamical diffraction theory [2] that describes the diffraction processes inside a perfect crystal, the intrinsic angular width of diffraction ω (Darwin width) must be taken into account, and therefore the energy resolution becomes

$$\frac{\Delta E}{E} = \cot\theta_B \sqrt{\omega^2 + \Delta\theta^2}$$

where ω is proportional to $\tan\theta_B$.$\Delta\theta$ depends on the geometry of the experiment. It is determined by the angular width of the beam upstream the monochomator and therefore by the angular width of the source to tan coupled with the preceding optics and distance to the source and on the perfection of the crystal. Crystals with imperfections have reflection widths much larger than perfect crystals. Assuming a perfect crystal such as, for instance Si(111) and a perfectly parallel beam, $\omega = 2.66 \times 10^{-5}$ rad at 10 keV and $\frac{\Delta E}{E} = \omega \cot\theta_B = 2.66 \times 10^{-5} \cot(11.4°) = 1.32 \times 10^{-4}$. Another important property of a monochromator is the intensity of reflection. There are two relevant quantities that must be distinguished: the reflectivity, i.e. the height of the Darwin width, and the integral reflecting power, i.e. the area under the Darwin width. The intensity of the reflected beam is determined by the latter when the angular spread of the incident beam is much larger than the Darwin width. Both the quantities are affected by crystal quality.

The standard method to obtain monochromatic X-rays of desired properties is to use multiple Bragg reflections. A double crystal monochromator with two parallel crystals produces a monochromatic beam running parallel to incident white X-ray beam. The scheme of a double crystal monochromator is shown in Fig. 3.5.

The whole system is mechanically designed in order to rotate the pair of crystals to change the incident angle corresponding to a given energy. While the direction of the incident and exit beam is the same, the vertical offset $\boldsymbol{h}$ between the incident and the exit beam changes with energy according to the relation

$$\boldsymbol{h} = 2g\cos\theta$$

where g is the distance between the two crystals and θ is the Bragg angle. The obvious way to minimize the changes of $\boldsymbol{h}$ with θ is to make the width of the channel g as small as possible. In order to make the position of the exit beam independent of θ, it is necessary that

$$g \sim \frac{1}{\cos\theta}$$

Energy variation is obtained by rotating the whole two-crystal assembly around a common axis. In such geometry, the reflectivity of the system is given by the convolution of the Darwin widths of the two crystals leading to a rapid falling off the tail intensity. In order to obtain monochromatic radiation with the maximum possible intensity an accurate parallelism between the two crystals is necessary. The constraints on the parallelism of the first and second crystals are determined by the angular emittance of the source and acceptance of the crystal used and is typically of the order of sub-μ rad. Generally a fine mechanical adjustment of the parallelism of one crystal with respect to the other is possible through a piezoelectrically controlled feedback circuit. Other conditions for the alignment of a double crystal monochromator are the parallelism normal to the scattering plane and to the rotating axis, which should be both better than 10^{-3}–10^{-4} rad. A kind of double crystal monochoromators are monolithic or grooved channel cut monochromators [3], having the additional advantage that both diffracting parts of the monochromator are naturally aligned. Double crystal monochromators in which rotation is the only movement, coupled with opportune mechanics and data acquisition strategies, can be successfully used for QEXAFS application i.e. EXAFS measurements in the subsecond regime implying an oscillation of the Bragg angle with up to 100 Hz in the EXAFS range [4–7].

A particular case of double crystal monochromators are the fixed exit double crystal monochromators, where not only the output direction is constant and parallel to the incident beam direction, but also the vertical beam position (offset) as the energy is varied [8–11]. To obtain the fixed exit monochromatic beam, the spacing between the two crystals is made dependent upon the Bragg incidence angle through a translation of one of the two crystals. A number of different schemes have been developed to realize fixed exit double crystal monochromators, such as those based on single or double cams. Figure 3.6 shows the double cam fixed exit double crystal monochromator from Kohzu (Japan) installed at the XAFS beamline at Elettra synchrotron source.

A different way to achieve the fixed exit of the monochromatic beam is given by the four bounce monochromators [12–16].

Moving one of the crystals slightly away from perfect parallelism can be used to reduce higher order energies that obey Bragg's law. As the Darwin width for higher energies is narrower, the lower energy selected by the first crystal is still within the Darwin width of the detuned crystal and therefore gets diffracted. For the higher order energies, on the other hand, the angle is now just outside the Darwin width, and therefore the photons are absorbed. For instance, in the case of silicon a misalignement of $\Delta\theta = 12\,\mu$rad produces 70 % of peak intensity for fundamental

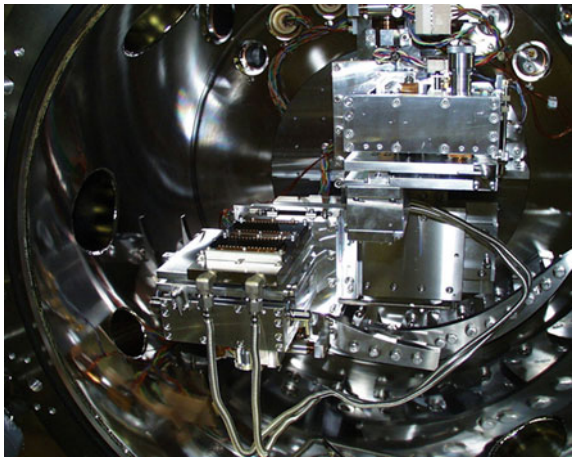

Fig. 3.6 Picture of the interior of the monochromator installed at the XAFS beamline at Elettra

reflection 111 at 10 keV and 0.3 % of peak for 3rd harmonic 333 reflection at 30 keV. A more efficient way to eliminate this issue is to use X-ray mirrors as high energy cut–off filters as discussed above.

In addition, the crystals of the monochromator can also be used to provide sagittal focusing. For this purpose bendable crystals have been developed. The crystal is mounted on a bending device in order to change the curvature of the crystal. As the angle of diffraction depends on the selected energy, also the curvature of the second crystal depends on the wavelength of the X-rays. A second bendable crystal, as the one installed on the MCX beamline at Elettra, has many degrees of freedom and as a consequence many remotely controlled movements. The number of degrees of freedom and the quality of the bending mechanism and the crystal results in a procedure for changing the energy that is not always straightforward [17].

As opposed to X-ray mirrors, crystals deflect at large angles, therefore they may be used to construct branchlines allowing photons to arrive at an alternative experimental station. Figure 3.7 shows a scheme of the SAXS beamline at Elettra [18]. The beamline uses the same source, a 57-pole wiggler, as the XRD1 beamline. The first crystal of the monochromator of SAXS intercepts a part of the beam. The remaining part of the beam continues its path indicated by the dotted line in Fig. 3.7 and goes to the optical and experimental sections of the XRD1 beamline. The part that is diffracted by the crystal finds a second parallel crystal one floor higher. After diffraction at the second crystal the beam continues a path that is parallel to the incoming beam, but several meters higher. As the difference in height between the first and second crystal is large, it is not practical to have a translating second crystal. In the case of the SAXS beamline, three different second crystals are installed, each at a specific position and at a specific angle. In this way three different energies can be selected for the experiment by changing the angle of the first crystal.

In general branch lines are often constructed with one crystal that partially intercepts the beam. When the beam is diffracted in the horizontal plane, usually a second

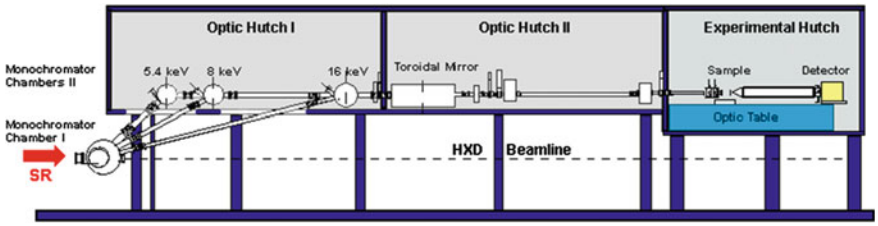

Fig. 3.7 Schematic representation of the SAXS beamline at Elettra

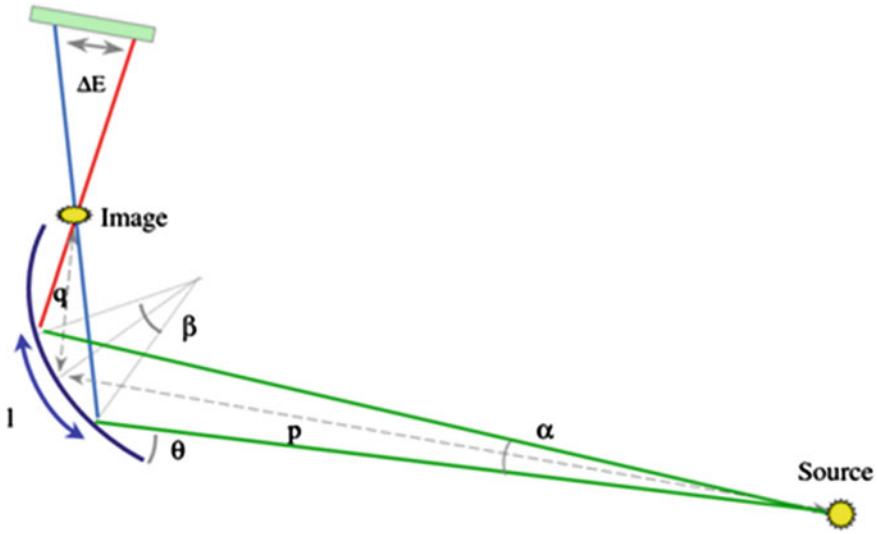

Fig. 3.8 Geometrical arrangement of the energy dispersive optics

crystal is omitted. The consequence of this is that the branch line has to work at a fixed energy, as changing the energy would imply having to move the branchline.

Besides double-crystal monochromators selecting one specific wavelength according to the incident angle, a single crystal polychromator can be used for X-ray to disperse different energies at different directions similarly to prisms for visible light. The geometrical arrangement of the energy dispersive optics is given in Fig. 3.8.

A quasi-parallel and polychromatic beam, supplied by a synchrotron radiation source, is energy dispersed and focused by an elliptically curved crystal. Because the incident X-rays strike the crystal at slightly different angles along its length, the bent crystal acts as a polychromator diffracting a different energy at each point. This energy-dispersed beam converges to a focus at the sample position. The beam, transmitted through the sample position, then diverges towards a position sensitive detector. The position of the beam, incident in the detector, can be directly correlated to energy. Considering a cylindrically bent crystal, which is a good approximation for an ellipse, the source to crystal distance p is large compared to the radius of

curvature R of the crystal. R is related to the source to crystal distance p, crystal to focal point q, and bragg angle θ for the central X-ray beam, through the equation of cylindrical optics:

$$\frac{1}{q} + \frac{1}{p} = \frac{2}{R \sin \theta_B}$$

The angular dispersion $\Delta\theta$ is:

$$\Delta\theta = \beta - \alpha = \frac{l}{R} - \frac{l \sin \theta_B}{p}$$

where l is the illuminated length of the crystal. The diffracted energy range is given by

$$\Delta E = E_H - E_L = E_0 \cot\theta \, \Delta\theta = E_0 \cot\theta \left(\frac{l}{R} - \frac{l \sin \theta_B}{p} \right)$$

where E_H and E_L are the highest and the lowest energies respectively, E_0 is the energy of the central beam.

Examples of dispersive EXAFS spectrometer are ID24 at the ESRF [19] and ODE beamline at SOLEIL [20].

3.2.2 X-Ray Detectors

One of the fundamental elements of the experimental station is the X-ray detector. Various types of X-ray detectors exist and the best choice is a trade-off between the nature of the experiment and the merits of different technological approaches. X-ray detectors can be either photon counting or integrating. Photon-counting detectors measure each individual X-ray photon separately, while integrating detectors measure the total amount of energy deposited in the active region of the detector. In general the detectors can be divided into three classes: (i) 1D detectors (or point detectors), (ii) position sensitive detectors, and (iii) energy dispersive detectors. The latter provide information on the energies of the detected X-rays. The position sensitive detectors give spatial information and the 1D detectors only give information on the X-ray flux. The field of X-ray detection is large and merits a chapter of its own. Here we will discuss the most important characteristics of detectors and give just one example of each type.

The parameters that are of universal applicability and permit the comparison of different detection systems are:

1. *Wavelength range*. The long wavelength limit is set by the minimum photon energy required to produce an event, while the short wavelength limit is typically set by the transmission of the window or protective coating of the detector.
2. *Detective Quantum efficiency (DQE)* defined as

$$(\text{signal}_{\text{out}}/\text{noise}_{\text{out}})^2/(\text{signal}_{\text{in}}/\text{noise}_{\text{in}})^2.$$

3. *Noise*. Fluctuations of the detected signal by different elements within the detector system limit the minimum-detectable signal level. Some of the more important sources of noise are:
    a. *Photon noise*. The number of photons arriving at a detector in a given time interval is subject to statistical fluctuations. If the number is N, then the standard deviation will be $\sqrt{N}$.
    b. *Dark noise.* It is given by the signal in absence of incident radiation. The dark noise is subject to the same statistical fluctuations as the signal from the incident photons. The *dark* si*gnal fluct*uations contribute to the overall noise of the system and may be a serious limitation at very low signal levels.
4. *Dynamic range*. It is expressed as the ratio of the maximum signal that can be measured before the onset of saturation effects, to the root mean square value of the intrinsic noise of the detector. The intrinsic detector noise is that corresponding to noise events which are registered as true signal events. A certain 'dead time' is associated with the detection of each event, and at high count rate, lost events results in non-linearity of response. In this case the detector is said to have reached saturation.
5. *Spatial resolution*. The ability of the detector to identify the position of arrival of the detected photons.
6. *Temporal resolution*. The ability of the detector to determine the time-of-arrival of the detected photons.
7. *Environmental requirements*. Special requirements needed for the correct operation of the detector (e.g. cooling, high vacuum, shielding from external magnetic fields).

One example of point detector is the ionization chamber in which a photon with energy greater than the ionization threshold is absorbed in the gas, producing an electron-ion pair. The overall detection efficiency will be a function of the quantum yield of the gas at a given photon energy, the number of photons absorbed in the total path length of the gas chamber, and the transmittance of the window material. The number of photons absorbed is defined by the Lambert-Beer law as:

$$N = I(1 - e^{-\sigma \varrho L})$$

where I is the intensity of radiation in the chamber (photons/s); L is the length of the chamber (cm); ρ is the density of atoms and molecules (cm^{-3}): and σ is the absorption cross section of the gas (cm^2). The number of electron-ion pair n produced is:

$$n = I_0 T \gamma (1 - e^{-\sigma \varrho L})$$

where I_0 is the intensity of the incident radiation, T is the transmittance of the window material, and γ is the photoionization yield of the gas. If a high voltage is applied to

the ionization chamber, than the primary electron gains sufficient energy during its transit through the gas to cause a secondary ionization. Under these conditions, the output current is amplified.

In diffraction and scattering experiments spatial information (the angle at which the X-rays are scattered) is very important. Position sensitive detectors are therefore commonly used as they provide a large amount of spatial- and intensity data in a relatively short time. An example of a position sensitive detector is the direct-detection pixel-based solid-state detector. In these detectors the X-rays (or electrons) directly hit a semiconductor, creating free electrons and holes that are detected by electronics. Read-out electronics are designed to have a low noise, a high dynamic range and a fast readout. X-ray pixel detectors built in hybrid design consist of a radiation sensor, a reverse biased pn-diode (usually silicon) with a segmented contact structure on the p-side, and a readout ASIC-chip, with the same pixel structure. Sensor and read-out chips are connected via tiny conducting indium balls, called bump-bonds. X-rays are detected in the sensor and the resulting signal is amplified in the pixel chip. When the detected charge reaches a certain threshold, a photon is counted. By adjusting the threshold value one can also exclude lower energy photons. In this way background resulting from fluorescence may be removed. Due to the direct detection of the X-rays with a silicon sensor, the spatial resolution of such detectors is excellent. The DQE is given by the absorption of the X-rays by the silicon, which is 80 % at 12 keV and even 100 % at 8 keV.

Other type of experiments may require detections of the various energies of the X-ray photons, e.g. fluorescence measurements. In this case energy dispersive detectors may be preferred. A silicon drift detector (SDD) is an example of such an energy dispersive detector. Silicon Drift Detectors are basically discs of n-type silicon. On the opposite side of the part that is exposed to the X-rays a transverse electric field is generated by means of a series of ring-electrodes. Electrons are generated in the silicon when X-ray radiation is absorbed. The electric field forces the electrons to drift in a sideways direction towards a small anode. The amount of electrons that reach the anode is proportional to the energy of the absorbed photon. The small size of the anode and the integration of the first FET of the amplifier electronics in the anode greatly minimize the capacitance of the detector giving a higher energy resolution and a higher photon count rate. The energy resolution is expressed in full width at half maximum (FWHM) and is typically 125–150 eV for Mn Kα wavelength ($\sim$2.1 Å).

3.2.3 Diffraction Beamlines: MCX at Elettra

The MCX (Material Characterization by X-rays) beamline at Elettra [21] allows to perform a wide range of non-single crystal diffraction experiments: grazing angle diffraction and reflectivity, residual stress and texture analysis, phase identification, structural and kinetic studies. Systems that can be investigated vary from organic and inorganic thin films, to thermally and/or mechanically modified surfaces of mechanic

components, to polymers, catalysts and highly disordered materials in the form of powders and fibers.

In order to fulfill the required flexibility in terms of beam characteristics at the experiment, ranging from spot focus to line focus and to parallel beam, the optics of the beamline consist of two mirrors and a monochromator: a first Pt-coated cylindrical mirror collimates the beam on the sagitally focusing Si(111) double crystal monochomator in 1:1 configuration. The second—meridional focusing—platinum coated mirror is flat and bendable, with a radius adjustable from 6 km to flat.

The fixed-exit double crystal monochromator (DCM) consists of two Si(111) crystals, which can be precisely positioned and oriented in the X-ray beam. The energy resolution is that inherent to Si(111). This fixed exit operation is obtained by placing the crystals on two independent rotation stages, and translating the second crystal along the beam direction. This crystal provides sagittal focusing; it is a ribbed crystal, cylindrically bent to a variable curvature radius.

The station has been designed to provide the maximum flexibility and easy use with reasonable precision and performance and is based on a 4-circle Huber goniometer in full circle configuration with a flat sample-holder plate (Ø 100 mm) controlled by a precision x-y-z motor system, 360° phi-rotation and $-90 \div +90°$ chi-tilting. The 2θ rotation is provided with an encoding system for accurate control and real-time feedback on the actual angular positions. The diffracted arm carries, as a default, a crystal analyzer/scintillation detector system.

3.2.4 Absorption Beamlines: the XAFS Beamline at Elettra

The Elettra synchrotron source hosts a spectrometer dedicated to XAS, the "XAFS" beamline [22], installed on a bending magnet source. It was designed to cover a wide energy range: from 2.4 to 27 keV meeting the needs of a large number of researchers in the area of conventional XAS. The optical layout is shown in Fig. 3.9.

The mask defines the size of the beam accepted by the collimating mirror. The mirror, placed at 16.5 m from the source provides vertical collimation and consists of a silicon ingot with platinum coating. It has an optically active length of 1,000 mm and width of 60 mm respectively and it is positioned at 3 mrad with respect to the direct beam. The mirror is water cooled and is operated under ultra high vacuum conditions. Two pairs of entrance tungsten alloy slits define the shape of the beam impinging on the monochromator. The monochromator, placed at 21.7 m from the source is a fixed exit double flat crystal double cam Kohzu apparatus. The energy range 2.4–27 keV can be covered using interchangeable under vacuum pairs of Si(111) and Si(311) crystals. The energy resolution is that inherent to Si(111) and Si(311). The fixed exit is achieved by the rotation and translation of the first crystal along the two cams. The detuning of the second crystal provides harmonic rejection at working energies below 9 keV. Downstream the monochromator a second set of tungsten alloy slits are used to define the beam on the sample. Any specialized sample environment set-up is mounted on a wide motorized table. The standard set-up allowed transmission mode

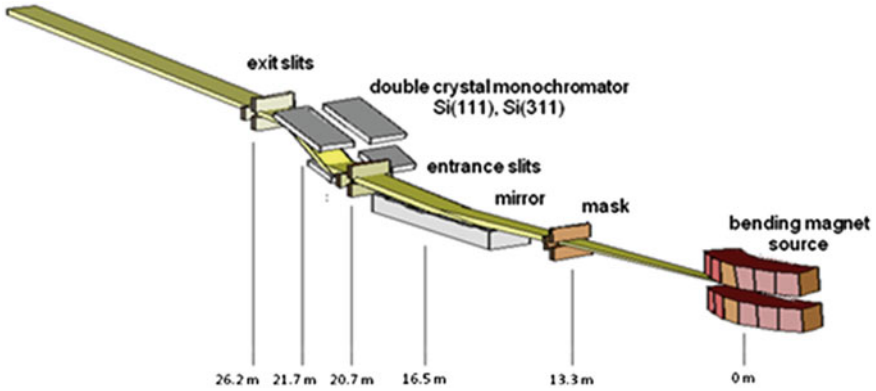

Fig. 3.9 Scheme of the optical layout of the XAFS beamline at Elettra

with ionization chambers for beam intensity measurements. These are filled with optimal He, Ne_2, Ar, Kr gas mixtures at a total pressure of 2 bars and are operated at a field of 2 kV per 30 cm of length. The ionization chambers signals are amplified and digitalized by a voltage to frequency converters before being finally read by the counters of the data collection PC. The typical photon flux at the sample for standard beam size and ring current is in the 10^{10} photon/s range. The noise level contribution due to the photon statistics in the normal transmission geometry can be therefore limited below the 10^{-4} level. A large-area Si drift detector is the standard device for fluorescence measurements.

3.3 Soft X-Ray and Vacuum Ultraviolet Beamlines

The absorption coefficient of optical materials makes the VUV and soft X-ray part of the spectrum very different from the visible and hard X-ray photons. In this energy range there are no windows, no optical lenses, no prisms, etc…, but only poorly reflecting mirrors. Even air is opaque to radiation in the 6–1,000 eV range. Thus, the entire optical system for a beamline must be kept under vacuum. Only at very small angles of incidence the reflectivity increases at a given photon energy (i.e. as the photon beam tends to become more parallel to the optical element surface).

Conversely, for the same reason, light in this spectral region is particularly sensitive to the electronic properties of matter. This is due to its strong coupling to valence electrons in the solid and to resonant processes at accessible core levels that can enhance the scattering amplitudes by orders of magnitude. Such phenomena lie at the core of the renewed interest in the exploitation of VUV and soft X-rays for the investigation of wide classes of materials including technologically relevant compounds, alloys, and advanced nanoscale materials.

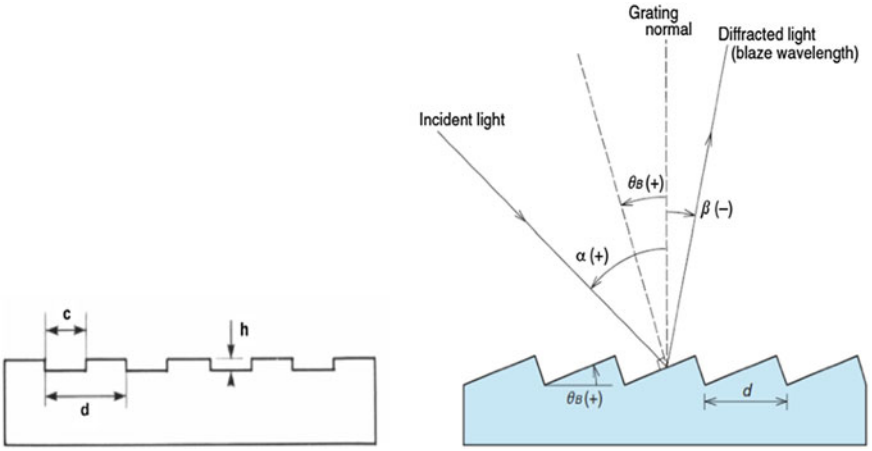

Fig. 3.10 Laminar (*left*) and blazed (*right*) gratings. The incidence α and diffracted β angles are defined

Furthermore, the wavelength of soft X-rays, from ~ 0.5 nm to a few nanometers, well matches with many interesting and useful length scales occurring in several materials either natural or engineered. However, those wavelengths do not allow the use of single crystals as monochromators, as done in the hard X-ray region. We need, therefore, to engineer gratings with well-defined line spacing and size using mechanical systems or holography in order to utilize the Bragg diffraction for monochromatization [23, 24]. Usually there are two kinds of grooves for gratings: blazed or laminar tooth profile as shown in Fig. 3.10. The notation adopted in Fig. 3.10 uses opposite sign of the angles α and β if they are on opposite sides of the normal. The Bragg grating equation may be written as $m\lambda = d\,(\sin\alpha + \sin\beta)$.

The distance d is the separation between lines, m is the order of diffraction. The angles α and β are both arbitrary, so it is possible to impose various conditions relating them. If this is done, then for each λ, there will be a unique α and β. The following conditions are typically used [25]:

- On-blaze condition:

$$\alpha + \beta = 2\theta_B$$

where θ_B is the blaze angle (the angle of the sawtooth).
The grating equation is then $m\lambda = 2d \sin\theta_B \cos(\beta + \theta_B)$

Fixed in and out directions (entrance and exit slits):
$\alpha - \beta = 2\theta$, where 2θ is the (constant) included angle.

The grating equation becomes $m\lambda = 2d\cos\theta_B \sin(\theta + \beta)$
In this case, the wavelength scan ends when α or β reaches 90°, which occurs at the horizon wavelength $\lambda_H = 2d\cos^2\theta$.

- Constant focal distance:

$\frac{\cos\beta}{\cos\alpha}$ a constant C, leading to a grating equation

$$1 - \left(\frac{m\lambda}{d} - \sin\boldsymbol{\beta}\right)^2 = \cos^2\frac{\beta}{c^2}$$

The typical experimental techniques in this energy range can be summarized as near-edge X-ray absorption fine structure (NEXAFS) spectroscopy, soft X-ray emission spectroscopy (SXES), resonant inelastic X-ray scattering (RIXS), X-ray magnetic circular dichroism (XMCD), X-ray photoemission spectroscopy, in all of its aspects (XPS, ARPES, Resonant XPS etc…), and Auger spectroscopy.

These types of spectroscopies exploit the excitation of electrons in relatively shallow core levels and valence band to probe the electronic structure of various kinds of matter. They are extremely demanding techniques because they require all the characteristics of a modern X-ray beamline at the same time, such as:

- Brilliance. The illuminated spot on the sample must be very small. The flux must be as high as possible because the cross sections of the processes are small. State of the art focusing and optics that transmit as much as possible the brilliance of the light emitted by the insertion devices are required.
- Resolving power. A total resolving power greater than 10^4 requires that the monochromator must work at least at 20,000 resolving power over the whole energy range in order to have photon energy resolutions of ten's of millielettronvolts.
- Stability. These experiments are intrinsically slow and long acquisitions are needed. The stability needs to be maintained when varying energy and polarization. Gains in the thermal stability of the beamline optics, as well as in the machine stability, will be directly reflected in the data quality.
- Polarization tunability. The source must be capable of delivering linearly and circularly polarized radiation with any orientation over the whole spectral range.

3.3.1 Soft X-Ray Energy Optics

In order to design a beamline featuring all these characteristics we must analyze the focusing effect of the optical elements (mirrors and monochromators).

Toroidal (spherical) mirrors [26] and gratings [27] are commonly used in beamlines working in the soft X-ray range, primarily because they are commercially available at low cost and because the number of optical element present in a beamline can be reduced, since in this case both mirrors and gratings can focalize the

beam. However, the beam image produced is poor having the dropping arc form due to astigmatism.

Parabolic mirrors [26, 28] can be used to collimate the synchrotron radiation in front of a plane grating and then to re-focus the scattered radiation on the exit slits of the monochromator. However it is difficult to manufacture these aspheric surfaces. Therefore, these optical elements have larger tangent errors and higher costs. Moreover, the fact that two of such mirrors are required for a monochromators is a further disadvantage for the use of parabolic mirrors.

Elliptical mirrors [26, 28] are also difficult to manufacture with small tangent errors, but the possibility to use two of them or one elliptical and one toroidal mirror in a Kirkpatrick-Baez (KB) design [28] (see the paragraph 5) allows one to have a system almost free of aberrations. In this geometry two mirrors are used before the monochromator, which independently focus the beam in the two orthogonal planes on the monochromator exit slit.

For the monochromator we can choose between spherical (toroidal) gratings, that have the intrinsic advantage to reduce the number of optical elements in the monochromator, or plain gratings that, instead, have the advantage to cover a larger energy range and to have typically higher resolution [29]. The resolution and flux (as well as the presence of high order diffraction lines) also depend on the blazed or laminar groove profiles. Blazed profiles typically have high-flux, but lower resolution and important high order diffraction lines. Laminar profiles shrink the flux but increase the resolution and have negligible high order diffraction lines [29]. The choice of blazed *vs* lamellar gratings and the optimization of their profile parameters determines the characteristics of a beamline. Due to glancing angles on the mirrors as well as optimized groove densities and profiles of the gratings, high photon flux can be achieved reaching up to 10^{13} photons/s/0.01%BW at 1 keV.

In the case of spherical or toroidal grating monochromator (SGM or TGM), a very simple solution is just to have the grating (or more gratings) as the only optical element between the entrance and exit slits. This solution is very cheap and in some cases may be a very good solution for photon energy in the VUV range (see the next paragraph). However, in many cases, the typical optics for SGM (TGM) are formed by a plane mirror and a spherical (toroidal) grating between the entrance and exit slits. These types of monochromators are severely limited by the fact that the gratings must also focus the entrance slit beam to the exit slit. This implies that the focus on the exit slits will change by moving the grating and this change may become too large in the soft X-ray range for practical purposes. Moreover, the energy resolution ΔE is proportional to the energy E, so at high energy it may be unfavorable.

For plain grating monochromators (PGM) typically one grating can be enough to cover a wide range of energy (50–1,500 eV). However, the optical design of the monochromator is more complicated than a SGM since it requires a plane mirror to send the beam on the plain grating and a refocusing mirror (usually elliptical mirror) after the grating to focus the beam on the exit slits. This conceptual design is called SX700 [30–32]. The resolving power $E/\Delta E$ decreases in a slower way with the increasing energy with respect to the SGM, given that it is proportional to $E^{1/2}$.

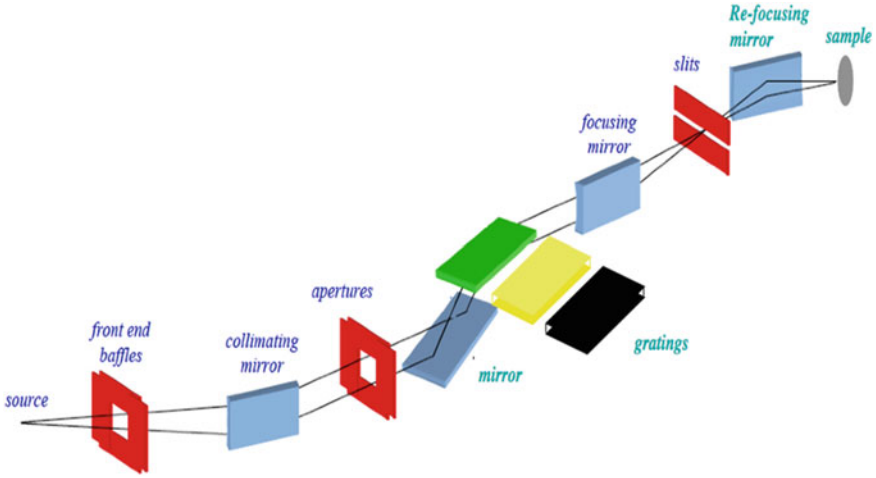

Fig. 3.11 Optical layout of a soft X-ray beamline based on the collimated-light PGM

3.3.2 Layout for a Soft X-Ray Energy Beamline

The conceptual layout of the optics of a soft X-ray beamline optimized for spectroscopy studies is shown in Fig. 3.11. This scheme is based mainly on the design of high-resolution soft-X-ray spectroscopy beamlines present in 3rd generation synchrotrons, like ADRESS [33] at SLS, SuperESCA at Elettra [34] or the beamline 4.0.2 at ALS [35].

In this case the optics is based on the proven scheme of plane grating monochromator operating in collimated light [36]. The frontend pinhole (baffles) selects the coherent cone of radiation coming from the insertion device. The collimating mirror (CM) is a toroid, which converts the divergent beam from the pinhole into a photon beam parallel in the vertical (dispersive) plane. This deflecting toroidal mirror is designed to collimate along the vertical direction and to focus the beam horizontally at the exit slit. The mirror is typically made of Si, glass, SiC or zerodur ® substrates coated with about 30 nm of some coinage metals. In Fig. 3.12 the reflectivity of some metals at different grazing incidence angles are shown. They show a good reflectivity up to 2.2 keV. We note that at the reported incidence angles (88–89°) the *s* and *p* reflectivity are almost identical. Therefore, the beamline will not distort circular polarized radiation.

The monochromator situated downstream consists of a plane mirror (PM) and selectable gratings, dispersing the beam in photon energies. The vertically collimated beam is deflected by the plane mirror illuminating the plane grating, at an angle of incidence α necessary to select the energy. This second optical element, the plane mirror PM, like the CM, is made of Si, SiC, etc… substrates coated by Au or Pt. Since the incidence angle of the monochromator must be moved to select different energies, the typical angular resolutions for the gratings are 0.03 and 0.05 μ rad for

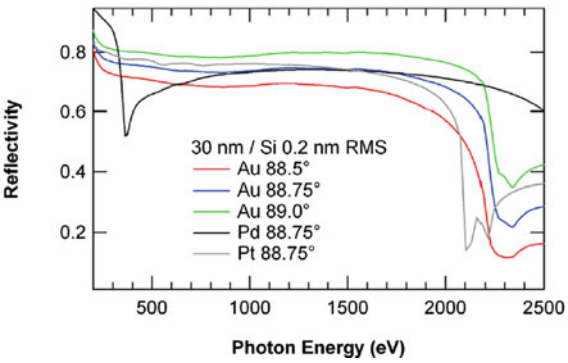

Fig. 3.12 Reflectivity of possible coatings for s polarized light as a function of the photon energy. The substrate is Si and the coating is 30 nm thick. The RMS surface roughness is 0.2 nm

the plane mirror. Since the angle of incidence on the mirror for a given grating is determined by the focusing condition and the grating equation at that energy, it is advantageous to have at least three gratings that allow exchanging resolution for flux, keeping a fixed exit slit width. In the proposed scheme three gratings with constant groove densities N in the possible ranges $300 < N < 1{,}000$, $1{,}100 < N < 3{,}000$ and $3{,}100 < N < 5{,}000$ l/mm are used to provide even coverage of the beamline resolution and transmission parameters.

However, the collimated light PGM [37] in general benefits from high resolution, high flux, due to absence of the entrance slit allowing the beamline to accept the whole coherent cone of undulator radiation, and wide energy range already covered with one single grating. In fact, large $\cos\beta/\cos\alpha$ values are used to improve resolution at the expenses of flux.

After the grating there is the focusing mirror (FM). FM is an elliptical cylinder mirror, which focuses the dispersed collimated beam on the exit slit of the monochromator, producing monochromatic light. In the horizontal (non-dispersive) plane, the FM has no focusing properties and, as explained above, the beam from the source is directly focused by the CM on the exit slit, producing a stigmatic focus. This collimated PGM design is almost free of aberrations.

Finally, the refocusing mirror (RM), that can have a toroidal or elliptical shape, refocuses the beam on the sample in the endstation. The angle of incidence on both mirrors is close to 88–89°. Examples of parameters of all optical elements can be found in [33, 34].

Typically these beamlines will achieve a resolving power $E/\Delta E$ between 5×10^3 to 10^5 in the photon energy range 100–1,000 eV with a 10 μm exit slit width and with RMS slope errors of 0.1 μ rad over ~100 mm on the plane optical elements. A spot size (vertical × horizontal) with FWHM of less than 10×100 μm^2 requires RMS slope errors of approximately 0.5 μ rad along the meridional direction. The photon flux at the sample (depending on resolution and gratings) is in general between 10^{11} to 10^{13} photons/s/0.01%BW.

Other possible optical layouts are reported in many books [29, 38] and are present in several synchrotron beamlines [39–42]. Since a beamline is intended for a

particular set of techniques, the knowledge of the requirements of the experimental methods used is necessary before building a beamline. In addition the available space is also an important point for choosing the optical elements.

In order to match the high resolving power asked for the soft X-ray beamlines, state-of-the-art optical elements are required and some unavoidable constraints must be respected. The horizontal source size is much larger than the vertical one and, therefore, is not used in the dispersion direction in high-resolution systems. The vertical source size in 3rd generation synchrotrons is about 40-200 μm at the pinhole, and since this size limits the resolution, the optics of the beamline should reduce this size to less than 10 μm at the exit slits of the monochromator. The mirrors can demagnify the source by a maximum of 8, so in many cases the monochromator should also contribute to the demagnification.

Spherical gratings typically have 1:1 demagnification or slightly magnify the source. Therefore, demagnification by mirrors is required and a vertical entrance slit must be used to cut the beam. A typical example of a beamline based on a spherical (toroidal) grating monochromator is shown in Fig. 3.13, where the demagnification and astigmatic corrections are made by the KB mirror before the monochromator and the refocusing mirror after the exit slit.

PGM monochromators typically demagnify the source by a factor of 6, therefore an entrance slit is not required (although it may be advantageous) and there are even less requirements on the demagnification of the mirrors. If long energy scans without a grating change and with high-energy resolution is required for the experiments, an optical configuration based on a PGM monochromator is preferable, as shown in Fig. 3.11.

3.3.3 Low Energy VUV (4–40 eV) and Visible-Infrared Beamlines

Probes that use this region of the spectrum are very well suited to elucidate bonding in solids, surfaces, and molecules and to investigate electron–electron correlations and velocities in solids, atoms, and ions. At the lowest end of this energy range (below 3 eV), visible, infrared, and terahertz spectroscopies can be successfully used to study vibrational modes and optical excitations. Below 40 eV a myriad of techniques exists such as angle-resolved photoelectron spectroscopy (ARPES), photon-ion spectroscopy, inelastic ultraviolet scattering spectroscopy (IUVS), Fourier transform infrared (FTIR) spectroscopy and microscopy, terahertz (THz) spectroscopy, photoelectron-photoion coincidence spectroscopy. Since THz and IR beamlines are described in Chap. 15 of this volume, here we will focus on the VUV beamlines.

For wavelengths above 30 nm normal incidence optical configuration can still be used as some materials present a reflectivity close to 30 %, which is not the case below 30 nm. Nevertheless, a reflectivity of 30 % does not allow a beamline configuration with numerous optical elements, if relatively high monochromator throughput has to be conserved. Therefore, single optics normal incidence monochromators (NIM) based on a slightly modified Rowland circle principle (off-plane) are chosen [43, 44].

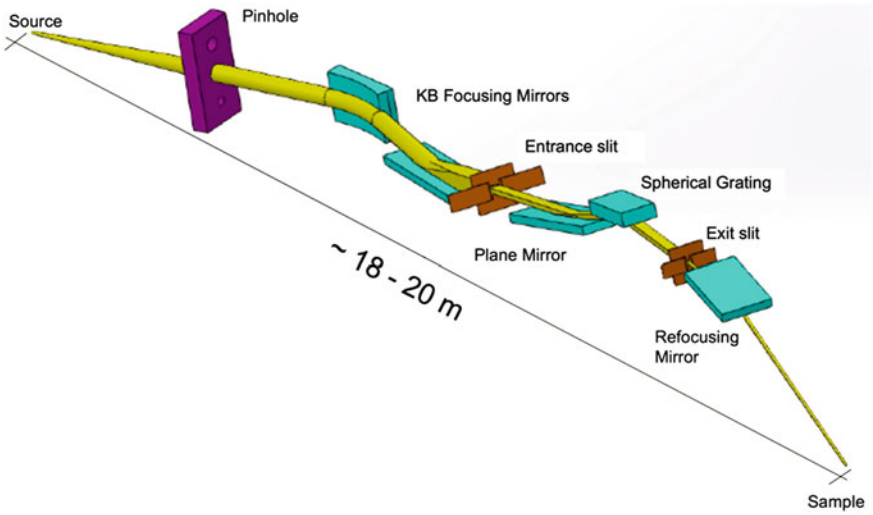

Fig. 3.13 Optical layout for a beamline based on a spherical grating monochromator and a KB focusing system. The total length is the typical distance from the source to the sample reported in m

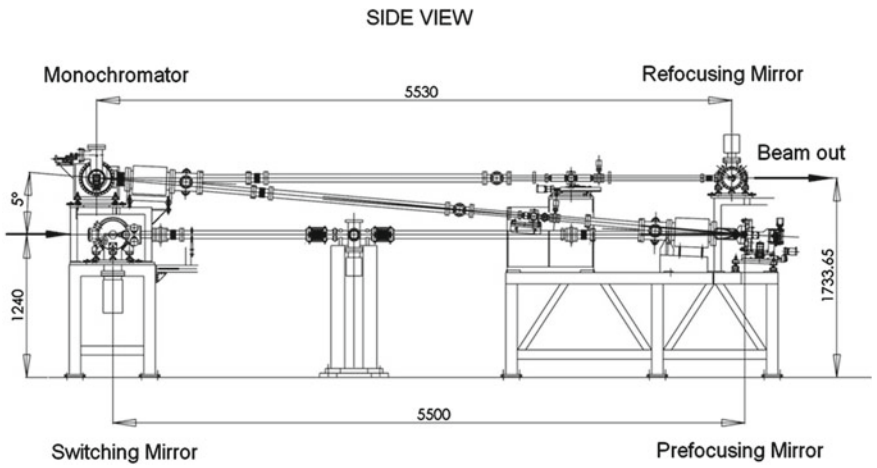

Fig. 3.14 Layout of the BaD ElPh beamline at Elettra. The distances are in mm

In this design a spherical grating is the only optical elements for the dispersion and focalization of light. The main difficulty in Rowland circle design is the non-constant position of the spherical grating focal point, which moves during the wavelength scanning.

The layout for a beamline based on a normal incidence monochromator, with 4-m-long focal length and constant included angle of 5°, is shown in Fig. 3.14 and

illustrates the BaD ElPh beamline at Elettra [45]. NIMs in this energy range offer the highest resolving power, but the photon energy range is restricted to a maximum of about 40 eV.

In this particular case, the light from the undulator is deflected towards the BaD ElPh beamline by a plane switching mirror, since this undulator serves two branchlines, BaD ElPh and IUVS (Inelastic Ultra Violet Scattering) [46]. The spherical prefocusing mirror upstream of the monochromator focuses the light onto the entrance slit. Due to the normal incidence, the demagnification factor of this mirror is about 14. The bare silicon portion of the surface of the mirror is used for photon energies up to about 11 eV, while the reflectivity of the Pt coated part is suitable for higher photon energies.

The monochromator is equipped with three exchangeable spherical gratings with efficiencies that are optimized for the photon energy ranges of about 4.6–13 eV (1,500 l/mm, laminar profile, Al/MgF_2 coated), 13–19 eV (3,000 l/mm, laminar profile, SiC), and 19–40 eV (3,000 l/mm, blazed profile, Pt coated). The groove profiles of the two laminar gratings (Al/MgF_2 coated and SiC) were designed to suppress the higher order diffraction efficiency. The Pt coated grating, designed to maximize the first order diffraction efficiency, has a blazed groove profile with a blaze angle of 3°. The exit slit distance from the gratings varies from 4,070 to 4,190 mm. This variation corresponds to the change in the vertical focal distance of the gratings moving from lower to higher photon energies. The last optical element of the beamline, namely the toroidal refocusing mirror, focuses the light onto the sample inside the experimental chamber. The parameters of the optical elements are given in Table 3.2.

The calculated resolving power ($\frac{E}{\Delta E}$) of the monochromator is shown in Fig. 3.15. The separate contributions from the slits, grating tangent slope error, and diffraction limit are presented for the 1,500 l/mm grating and for the 3,000 l/mm grating. The entrance slit is completely open while the exit slit is 10 μm. For each grating, the tangent slope error used for the calculations was 0.5 μ rad rms.

The photon flux of the BaD ElPh beamline (see Fig. 3.16) has been measured using a removable photodiode, located between the refocusing mirror and the endstation. With a pinhole of $4.5 \times 6.1\,mm^2$, slits width of 300 μm, and with 200 mA accumulated in the storage ring, the maximum photon flux, reached at 9 eV in first harmonic, is more than 5×10^{12} photons/s, while at 6.5 and 11 eV it decreases to about 1×10^{12} photons/s. For the SiC grating the maximum flux of more than 3×10^{11} photon/s is reached at about 20 eV. For the Pt grating the maximum photon flux, reached at 23 eV, is more than 1×10^{12} photons/s, while at 19 and 35 eV it decreases to about 3×10^{11} photons/s.

Other undulator-based NIM beamlines optimized for low-energy high-resolution ARPES with comparable resolving power and/or flux are present in other facilities like SSRL, SRC, NSLS, HiSOR, and BESSY [39, 47–53].

Table 3.2 Components of the BaD ElPh beamline [45]

Optical element	Distance from source center(mm)	Optical parameters	Incident angle to surface	Material	Coating
Source	0	Figure-8 undulator		NdFeB	
Pin hole	11,490			CuOFHC	
Heat loader	15,800	Plane	6°	GlidCop	Au
mirrors	16,400	Plane	6°	Si	None
Switching mirror	21,000	Plane	8°	Si	None
Prefocusing mirrors	26,500	Sphericeal R = 3,444 mm	87.5°	Si	None&Pt
Entrance slit	28,340			Strainless steel	
Three Gratings	32,160	Spherical			
Deviation angle = 175°		R = 4,038 mm 1,500 l/mm 3,000 l/mm Laminar		Silica SiC	Al/MgF_2 None
		R = 4,007 mm 3,000 l/mm Blazed		Silica	Pt
Exit slit	36,230–36,350			Stainless steel	
Refocusing mirror	37,690	Toroidal R = 13,000 mm ρ = 150.1mm	6.17°	Silica	Au
Sample	39,090				

Because of the use of a particular undulator and the presence of cooled heat load mirrors before the switching mirror, the power on the optics is strongly reduced and the monochromator is not cooled

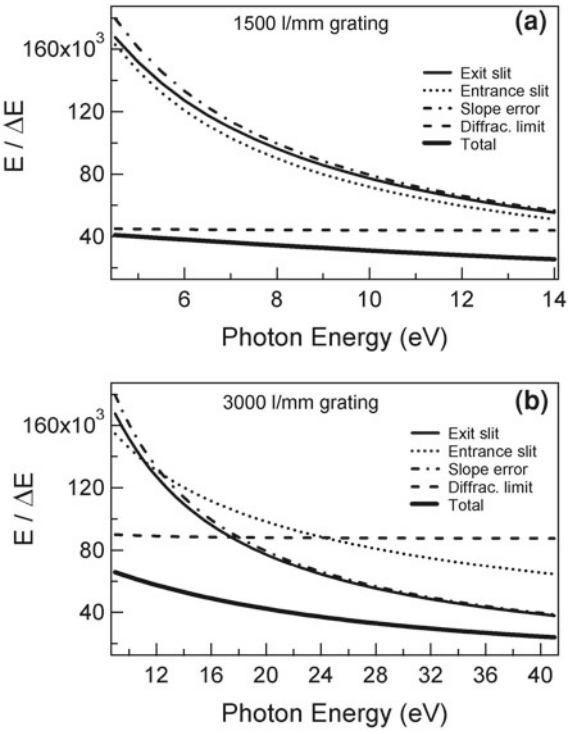

Fig. 3.15 Calculated partial and total resolving power, in first diffraction order, of the BaD ElPh NIM for the 1,500 l/mm (**a**) and 3,000 l/mm (**b**) gratings

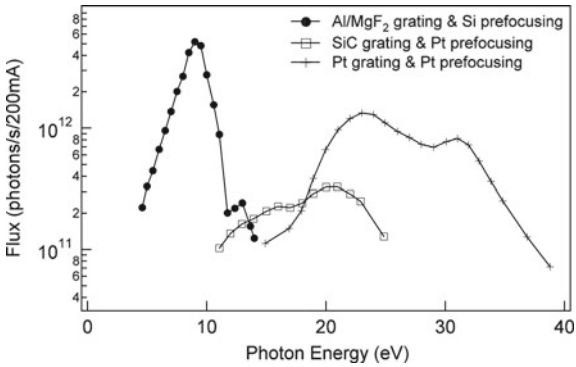

Fig. 3.16 Photon flux of the BaD ElPh beamline [45] measured with a photodiode using entrance and exit slit widths of 300 μm, and with 200 mA of electron current accumulated in the storage ring. In these experimental conditions the typical resolving power was around 2,500

3.3.4 Experimental Examples to Test the Beamline Performance

Absorption spectra of noble gases are typically considered to test the maximum energy resolution of the soft X-ray beamlines. Here we show the measurements made on the BaD ElPh beamline where the spin-orbit autoionization spectra of Ne gas between the $^2P_{3/2}$ and $^2P_{1/2}$ thresholds have been recorded via gas phase ion

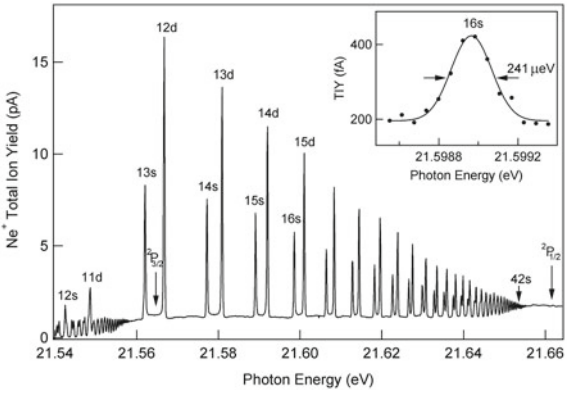

Fig. 3.17 Ne autoionization spectrum, measured with the 3,000 l/mm SiC grating in second order and with 20 μm exit slit width, showing an energy resolution of 310 μeV. *Inset* (*dots*) 16 s resonance spectrum recorded with 10 μm exit slit and (*solid line*) Gaussian fitting curve showing a FWHM of 241 μeV. The ionization energies for the formation of Ne^+ in the $^2P_{3/2}$ and $^2P_{1/2}$ states are also indicated

yield measurements. Above the ionization potential Ne^+ $^2P_{3/2}$, two Rydberg series 2p5ns and 2p5nd converge to the spin-orbit-excited Ne^+ $^2P_{1/2}$ ionization limit [54]. These Rydberg states are long-living with a very narrow natural line widths. As a result, using the neon spectrum the resolution of the monochromator can be observed directly from the line shapes of the Rydberg resonances [55].

The total ion yield measurements were performed with a gas cell, which is an integral part of BaD ElPh end-station.

In Fig. 3.17 we present a selected Ne^+ autoionization spectrum between the two 2p thresholds, showing the s and d Rydberg series, that has been calibrated on an absolute energy scale according to [56]. This spectrum has been recorded with the 3,000 l/mm SiC grating, operating in second diffraction order, with 20 μm of exit slit width and a completely open entrance slit (spot size at the entrance slit of about 7 μm). The observed FWHM of the neon 16 s resonance is 310 μeV, providing a resolving power $\frac{E}{\Delta E}$ of 69,000 at 21.6 eV in second order. This high resolution, together with the long-term stability of the entire beamline and of the electron beam in the storage ring, allows the observation of Rydberg states up to the 42 s level. The sharp and strong peaks below the $^2P_{3/2}$ threshold are due to collision-induced ionization in the neon gas. The inset of Fig. 3.17 shows the 16s spectrum, recorded with 10 μm of exit slit. The corresponding FWHM is 241 μeV, providing a resolving power of 89,000. In the above condition, with the grating operating in first diffraction order at 21.6 eV, the resolving power is 40,000.

Because the BaD ElPh beamline is connected to an end-station primarily devoted to ARPES [57, 58] from solids, which is common to many beamlines in the VUV and soft X-ray range, we briefly describe the main characteristics and some results of the corresponding end station in particular for the low photon energy regime. With respect

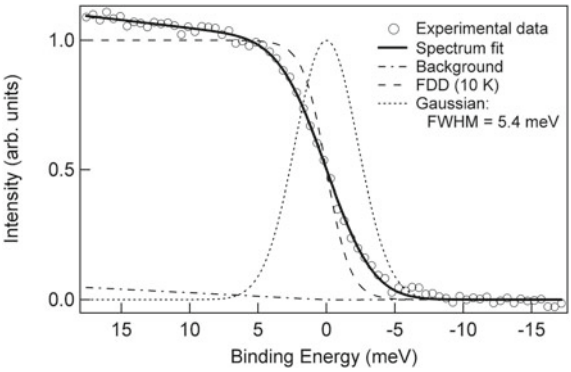

Fig. 3.18 Raw Fermi-edge photoemission spectrum from polycrystalline silver (*open circles*) and the fit of the data (*solid line*). The spectrum was measured at 10 K with a photon energy of 7.8 eV

to high-energy ARPES, the low energy counterpart offers great advantages in terms of energy and momentum resolution. Moreover, low photon energies provide enhanced bulk sensitivity, since the inelastic mean free path is expected to increase drastically for the electrons with kinetic energies below 10 eV [59], and are useful for tuning matrix elements, which vary rapidly at low energy. The universal demand in this area is for a high signal rate with very high resolving power. The high brightness and small spot size achievable with synchrotron radiation, particularly at third-generation sources and operation of very advanced monochromators, permits the design of new spectrometers, and electron energy analyzers with very high resolution.

In fact, the main part of the analysis chamber is the hemispherical 150 mm electron energy analyzer with a 2D-CCD detector system. This commercial 150 mm mean-radius hemispherical analyzer is mounted in a fixed geometry with an angle of 50° relative to the synchrotron radiation direction. The angular dispersive plane of the analyzer coincides with the polarization plane of the synchrotron light in first harmonic. The use of a 2D-CCD detector offers the possibility of simultaneous acquisition of the energy as well as the angular distributions of the photoelectrons. The span of $k_{||}$-vectors simultaneously probed by the analyzer is defined by the angular acceptance of the particular lens mode and by the photon energy. The maximum angular acceptance is about $\pm 17°$; moreover, an ultimate angular resolution of about 0.05° could be achieved.

The energy resolution in photoemission experiments is defined by the energy spread of the photon beam and the transfer function of the electron analyzer. For solids, it can be conveniently determined by measuring Fermi edges of polycrystalline noble metals at low temperature. Figure 3.18 shows a photoemission spectrum of the Fermi-edge of polycrystalline silver at 10 K acquired at the photon energy of 7.8 eV together with the fit of the data and its components. The exit slit of the beamline was set to 300 μm, while the entrance slit and the pass energy of the analyzer were set to 0.5 mm and 1 eV, respectively. The fitting function was the product of a linear background with the Fermi-Dirac distribution at the experimental temperature convoluted with a Gaussian. As a result of the fit the FWHM of the Gaussian, i.e. the combined experimental resolution of the beamline and analyzer, was found to be

5.4 meV. Under the above conditions, the calculated energy resolution of the BaD ElPh NIM is 2.4 meV. Therefore, an energy resolution of 4.8 meV can be estimated for the electron analyzer.

Finally, we note that on the experimental chamber of the soft X-ray and VUV beamlines, the sample must be mounted on a manipulator that typically has six degrees of freedom (three translations and three rotational axis). The sample holder, capable of accommodating transferable samples, is mounted on a cryostat that reaches, with liquid helium, temperatures lower than 10 K.

3.4 Cooling of Optics and Other Beamline Parts

Thermal considerations dominate the design aspects of modern optics and monochromators in view of the extremely high power and power densities of the insertion device beams of third-generation synchrotron sources. Typically the total power emitted from sources is in the order of 2–3 kW, while on the first optics after the pinhole it is reduced by one order of magnitude (about 150 W on an area of $2 \times 1.5\text{mm}^2$), but with the new superconducting and *in-vacuum* undulator a power density of >300 W can be reached.

It is clear that thermal issues are associated not only with the first optic that is impacted by the direct beam, but also with all the optics up to the monochromators and eventually slits, filters and shutter before the monochromator. To properly handle the incident heat load on these optics and beamline parts requires special measures, usually internal cryogenic cooling or the use of external water or liquid nitrogen cooling.

Filters can be used in the hard X-ray regime to attenuate the low-energy portion of the spectra, thereby reducing the power load on the following beamline components. Most existing filters are based on very thin layers of pyrolytic graphite, arranged in a stack in such a way that each filter absorbs a particular amount of power. The power is predominantly thermally radiated away by each graphite layer. Such filters can reduce the incident power by as much as 60–70 %. An alternative choice of filter material is CVD diamond, which can also be used as a vacuum window material.

Slits, used to define the beam dimension, are now very standard components of beamlines and are available either as independently adjusted jaws or as apertures of fixed widths (horizontally or vertically) that can be positioned anywhere in the beamline. It is prudent to place slits between successive optical components, as well as near the downstream end of the beamline. Commercial versions are available and the slits positioned before the monochromator (pinhole, entrance slit etc…) must be cooled.

Every beamline will have at least one pneumatically actuated photon shutter placed downstream the source. Shutter designs, material and shielding will vary to meet the needs of individual beam sources and to handle the radiation spectrum that the shutter will confront. Whereas copper might be acceptable as a shutter material

if only synchrotron radiation must be stopped, heavier materials such as tungsten alloy would have to be considered if bremsstrahlung radiation must also be stopped.

The implications that thermal issues have on the brightness of the diffracted beam can be treated individually for each component factor of the brightness. Flux, relative wavelength spread and angular spread are impacted in a negligible way by thermal distortion and slope error variation (less than 2 %), but careful attention must be paid to the position spread of the diffracted beam. Thermal slope errors of monochromator planes have the same blurring impact on the beam dimension in the vertical plane as mirror figure errors would. It is determined by twice the RMS slope error multiplied by the distance from the monochromator. The effect of a 6 μ rad RMS thermal slope error is a blurring of the beam dimension by 240 μm at a distance of 20 m downstream of the monochromator. These effects might be significant, given that existing state of the art focusing mirrors (with figure errors of 2 μ rad or less) will attain vertical focus sizes less than 50 μm. Thus, cooling of monochromators is important to preserve most, but not all, of the aspects of the beam brightness. In some cases, to compensate the impact of the monotonic thermal distortion variation on the position spread of the diffracted beam in the vertical direction, it should be feasible to mechanically adjust, only slightly, the curvature of the vertical focusing mirror that would typically be used downstream of the monochromator. Considerable cooling must be provided to the mirrors before the monochromator to avoid deformations of the ideal mirror shape. The cooling needs to ensure that the heat-induced meridional RMS slope errors are below 0.5 μ rad.

In the case of high-energy X-ray beamlines that use a double crystal monochromator, the heat load on the first crystal must be taken into account, as more than 99.9 % of the photon flux from the source is being absorbed. The power deposited by the synchrotron radiation sources must be efficiently removed. The head load produces a temperature rise ΔT leading to a crystal d-spacing change $\Delta d = \alpha \Delta T$ where α is the thermal expansion coefficient. If a miss-matching between the first and the second crystal is produced, thermal drifts, loss of intensity and brightness and broadening of the beam may occur. Solutions for crystal cooling should take into account (i) the thermal expansion of the crystal α, (ii) the thermal conductivity in the crystal κ, and (iii) the heat transfer to coolant and crystal holder. Good cooling strategies are obtained for large $\frac{\kappa}{\alpha}$ ratios, large contact area between crystal and coolant/holder and of course if small power density is distributed over a large area. Typically this is achieved using water or liquid nitrogen circulation. Sometimes also closed-cycle circulating gaseous helium is used. This last option is employed, for example, on four existing NSLS insertion device beamlines.

3.5 X-Ray Optics for Microscopy

Visible and electron microscopies dominated for a long time the microscopy field. The former allows imaging thick samples with sub-micrometer lateral resolution in their natural aqueous environment, an appealing feature especially for the analysis of

biological specimens. Conversely, electron microscopes can provide sub-nanometric lateral resolution but they are limited to the imaging of thin samples in vacuum environment. X-ray microscopy covers the gap between visible and electron microscopy. The short wavelength and high penetration depth of X-rays offer the chance to image thicker samples, at few nanometer lateral resolutions, and even better. Despite X-ray imaging potentialities are known from almost one century, X-ray microscopes are among the latest developed in the microscopy field but nowadays they are becoming more and more popular in many 3rd generation synchrotron facilities. Indeed, they benefit from high brilliance, low emittance and coherence properties of X-ray synchrotron emission, but also from the technical advances achieved in the fabrication of X-ray optics, in detector performances and imaging modalities.

An X-ray microscope basically provides morphological and chemical information on the sample, and the image contrast is given by the specific interaction of the analyzed specimen with X-rays, a topic extensively detailed in Chaps. 13, 14 and 22 of this volume (for more details see also [60–62]).

3.5.1 X-Ray Focusing Optics

Generally speaking, there are three different geometries of X-ray microscopes: X-ray projection microscopes, Transmission X-ray Microscopes (TXM), also known as full-field transmission X-ray microscopes, and Scanning Transmission X-ray Microscopes (STXM). Here we focus on X-ray optics, on their working principle and on the technological progress toward nanoscale X-ray imaging.

Each focusing optical element is characterized by several parameters, which could be helpful to briefly remember at this stage: Magnification (M), Numerical aperture (NA), Resolution (Res), Depth Of Focus (DOF) and chromatic aberration. The optical magnification is a dimensionless number given by the ratio of the image size of the objected on its real size. For the Thin-Lens Equation, defined as p and q the source and image distance from the lens respectively, $M = \frac{q}{p}$. This implies that linear demagnification capabilities of X-ray microscopes can be improved by reducing q, and therefore, the optical focal length *f*, or increasing p, that is building longer beamlines. For synchrotron radiation, micro- and nano-probes are characterized by M$\sim 10^{-2}$–10^{-4} [63]. The numerical aperture of a focusing lens is a dimensionless number that measures the light gathered power. In air/vacuum $NA \sim \frac{r}{f}$, where r is the lens radius. NA is closely related to the photon flux at the focal spot, F, to the diffraction limited Res as well as to DOF. As a matter of fact, for the Liouville's theorem, $F \sim B \cdot \sigma^2 \cdot NA^2$, where B is the source brightness and σ the spot size. It clearly pops up that bright sources and large NA optics enhance the signal to noise ratio (S/N), lowering the detection limits. Lateral resolution, that defines the smallest resolvable sample feature, and depth of focus, that determines the maximum sample thickness in 2D imaging and sampled volume in tomography, are both inversely proportional to NA:

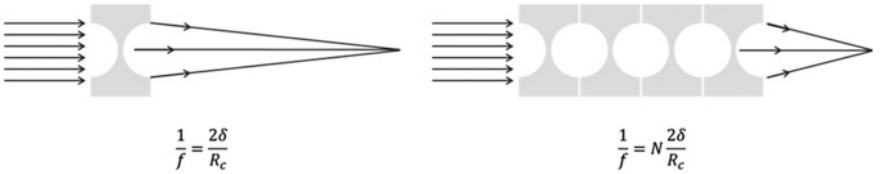

Fig. 3.19 Layout of refractive X-ray optics. **a** Single concave X-ray lens with focal length *f*. Rc is the lens curvature radius and δ the phase shifting part of the refractive index of the lens material. **b** Compound concave lens made of N single lenses having the same characteristic of (**a**)

$$Res = 0.61\frac{\lambda}{NA} \; for \; the \; Rayleigh' \; criterion$$

$$DOF = \pm\frac{\lambda}{2NA^2}$$

Chromatic aberrations introduced by a focusing element depend on the type of optics employed, that can be refractive, reflective of diffractive for X-rays.

Refractive optics were considered not particularly useful and quite impractical for X-ray focusing for long time. Since the real part of the refractive index for X-rays for all materials is slightly less than one in air or vacuum, X-ray focusing lenses must have a double concave shape and outstanding curvature radius. Indeed, for the Lensmaker's equation, the focal length would be of several hundreds of meters considering lens curvature radius in the range of few centimeters. Nowadays, compound refractive lenses (CRLs) are used. These are a series of concave lenses (see Fig. 3.19), first proposed in the 1996 by Snigirev and coworkers [64]. In order to increase CRLs' efficiency by limiting X-ray absorption, CRLs should be made as this as possible and fabricated with high density, low Z number materials, such as aluminum, beryllium, carbon (diamond or graphite), silicon, boron or lithium.

In 2002, CRLs made by N = 120 parabolic single lenses of polycrystalline aluminum (f = 1048 mm) were proposed and tested at the beamline ID22 of ESRF [65]. The tomogram of a microprocessor test sample has been obtained with a resolution slightly above 400 nm from the 3D rendering. In 2003, planar silicon parabolic CRLs with focal distances of few millimeters have been proposed and fabricated by using e-beam lithography and deep trench reactive ion etching, techniques that permitted to achieve the micrometric radius of curvature needed for shortening the focal length [66]. By exploiting a cross geometry for producing a 2D focus, two CRLs were used to generate at 25 keV at a distance of 42 m from the source (ID22 beamline at ESRF) a microbeam having a FWHM beam size of 210 ± 50 nm and 380 ± 90 nm in the horizontal and vertical plane respectively. By using planar silicon CRLs with similar design, a monochromatic hard X-ray beam (E = 21 keV) has been focused in a 47 × 55 nm^2 nanospot at the beamline ID13 at ESRF [67].

The major advantages offered by CRLs are the manufactory simplicity, with respect to reflective and diffractive X-ray optics, the low cost, the small size and

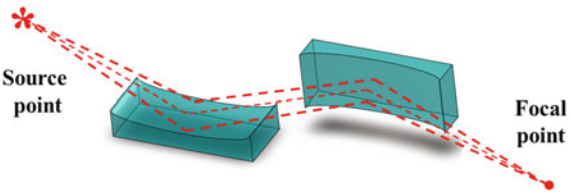

Fig. 3.20 Sketch of Kirkpatrick-Beaz mirror layout

alignment simplicity, the focal length tunability by simply adding or removing individual lenses and the low sensitivity to heat loading. Therefore, despite the absorption-limited efficiency, that makes them not useful in the soft X-ray regime, and the strong chromatic aberrations that affect them, CRLs are quite promising hard X-ray focusing elements and they have been recently used for imaging purposes [68].

With respect to reflective optics, it is well known that X-ray reflection efficiency is enhanced when working at grazing angle incidence, lower than the critical angle Θ_c, typically lower than 5° for soft X-rays. Grazing incidence reflective mirrors have been largely employed for hard X-ray focusing in SR facilities and still they are. In order to decrease the focal spot size, the reflector geometry mostly employed nowadays is indeed based on the use of two orthogonal elliptical grazing mirrors, which allow the successive focusing of the X-ray beam in the vertical and horizontal plane. This configuration, shown in Fig. 3.20, is known as Kirkpatrick-Baez system, first proposed in the 1948 [28]. Despite the relative simplicity of the working principle, efficient KB mirrors impose tight manufacturing constraints for both mirror shape and finishing. Shape errors introduce image aberrations worsening the achievable resolution while surface roughness affects mirror contrast and throughput due to scattering effects [69]. The shorter the X-ray wavelength being focused, the more precise the mirror surface must be. Technological advances over the years allowed improving both the precision of the figure shape and the surface smoothing.

The KB system can be either static or dynamic. In the static configuration, an elliptical shape can be obtained from a spherical mirror by differential polishing or differential profile coating [70, 71]. The mode of operation of static KBs is relatively simple and well suited for short radius ellipses. However, the fabrication technology is very expensive and KBs are optimized for a single set of working conditions, i.e. angle of incidence and focusing distance. Dynamic KBs are obtained bending flat mirrors by mechanical or piezoelectric actuation [72]. Dynamic KBs are less expensive than static KBs. They can be produced with a lower roughness and they allow the easy and fast tuning of focusing parameters, but they are not suitable for achieving very short curvature radius.

First KB mirrors were manufactured on glass or quartz substrates and coated with a reflective metal film. Nowadays, they are typically made from silicon crystals polished to near-atomic smoothness (micro-roughness lower than 3 Å) and then coated with ultra-thin layers of hard silicon carbide or dense metals. Multilayer coatings make possible to cover a wide spectral range, from 2 to 90 keV [73]. The improved manufacture capabilities came with advances in mirror cooling system and

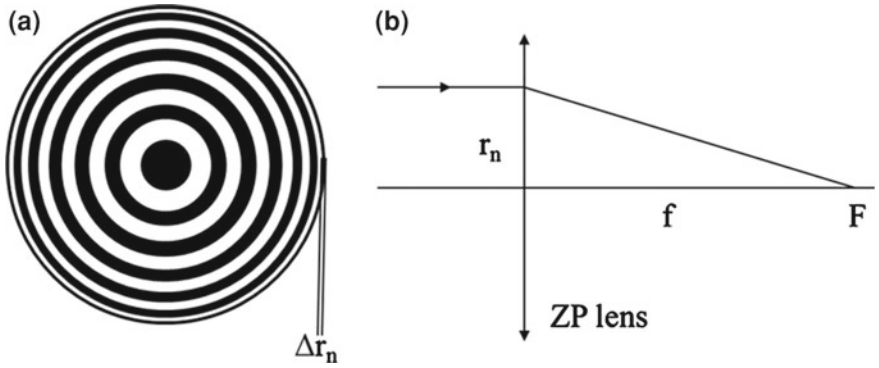

Fig. 3.21 Sketch of a Fresnel Zone Plate (FZP) **a** Zone plates are circular diffraction gratings with radially increasing line density. $\Delta\, r_n$ is the width of the outermost n zone. The central absorbing region, known as stopper, suppresses the strong zero-order diffraction. **b** Geometry for calculating the radius of the *n*th zone, r_n; n is the zone number; f is the focal length and F the focal point

positioning control. Actually, mirror deformation/degradation induced by heat load and tiny errors in axis adjustment would vanish any shape/finish upgrade.

KB mirrors have low chromaticity, which makes them particularly useful for spectroscopy purposes since the incident beam energy can be tuned without the need to adjust the focus on the sample. Resolution of several tens of nanometers has been achieved by exploiting KB systems [74] while the 10 nm resolution barrier has been overcome in more recent years operating an upstream deformable mirror and a multilayer coated KB mirror pair at 20 keV, a system installed at BL29XUL, the 1-km-long beamline of SPring-8 [75].

If KB geometry is the one mostly employed for hard X-ray focusing, the majority of soft X-ray microscopes exploit the focusing capabilities of diffraction optics, in particular the Fresnel Zone Plate (FZP). For this reason, we will devote more attention to their working principle, design, and performances. It has to be highlighted that a complete treatment of ZP theory if far beyond the purpose of this short section, and the reader is refereed to [76].

Figure 3.21 shows the geometry of a FZP. It is made by an alternate sequence of absorbing (black) and transmitting (white) regions, the width of which progressively decreases from the ZP center to the outermost region. The basic idea behind the ZP design can be explained retrieving the constructive interference conditions for a plane wave that illuminates a FZP made by n zones, having radius r_n and outer zone width Δr_n. For a given wavelength λ, in order to have constructive interference for the beams coming from the open zones of the ZP, the optical path difference between two adjacent open zones must be an integer multiple of λ. Being f the first-order focal length, considering the sketch in Fig. 3.21b, it follows:

$$f^2 + r_n^2 = \left(f + \frac{n\lambda}{2}\right)^2 \tag{3.1}$$

$$r_n^2 = n\lambda f + \frac{n^2\lambda^2}{4} \tag{3.2}$$

Neglecting the quadratic term of the expansion, which correspond to spherical aberrations [76], (3.2) can be approximated as:

$$r_n \approx \sqrt{n\lambda f} \tag{3.3}$$

Equation (3.3) defines the focusing condition for a ZP, and shows that a single ZP can focus well for a range of wavelengths, while the focal length increases with decreasing λ. Therefore, ZP lenses have very high chromaticity and incoming beam monochromaticity is mandatory for achieving diffraction-limited resolution. From (3.1) to (3.3), the fundamental parameter describing a zone plate can be retrieved. Defined as Δr_n the width of the nth zone, it is

$$\Delta r_n = \frac{r_n}{2n} = \frac{\lambda f}{2r_n} \tag{3.4}$$

From (3.4) it derives that the surface area of each ZP's zone is the same (i.e. $\pi\lambda f$), once the wavelength and the focal length are fixed. Therefore, each zone contributes equally to the focus intensity.

A ZP has m diffraction orders (being m an odd integer) that lead to multiple focusing points at distances f/m with respect to the optical element. When a zone plate is used as focusing lens, usually the first diffraction order is exploited and all other orders are blocked by a stopper for zero order and suitable Order Sorting Apertures (OSA) for higher ones. Negative diffractive orders also exist, so that a ZP can be operated also as a disperse lens.

The numerical aperture of a ZP can be estimated as in the following:

$$NA = n_{mat}\sin\theta \approx n_{mat}\frac{r_n}{f} = \frac{m\lambda}{2\Delta r_n} \tag{3.5}$$

where n_{mat} is the real part of the refractive index of the medium where the ZP is, Θ is the entrance acceptance angle of the zone plate and m the diffraction order considered, assumed n_{mat} close to 1 and small acceptance angles. Both conditions hold true under standard FZP working condition for X-ray microscopy. On the basis of the Rayleigh-criterion, the ZP spatial resolution δ_{ZP} can be calculated as

$$\delta_{ZP} = 1.22\frac{\lambda}{2NA} = 1.22\frac{\Delta r_n}{m} \tag{3.6}$$

From (3.6) the focal spot dimension decreases with decreasing the width of the outermost absorbing ring and at diffraction orders higher than 1. Conversely, FZP efficiency (i.e. the fraction of the incoming radiation diffracted into a focal spot) decreases by increasing m. A qualitative explanation of the ZP efficiency can be easily understood. First it has to be considered that opaque zones absorb part of the incoming

radiation. Since the fraction of the opaque zones is almost 50 %, it is possible to demonstrate that ∼50 % of the incoming radiation is lost by absorption. Moreover, 25 % of the incoming radiation is just transmitted by the FZP, or better focused at infinite distance for $m = 0$. The remaining 25 % of the focused power is divided among odd focusing order with efficiency inversely proportional to the diffraction order. Actually at the first order the efficiency is about 10 %. By "replacing" the absorbing rings with phase-reversing zones, the thickness of which introduces a phase change of π while minimizing absorption, theoretical ZP efficiency may be improved up to 40 %, since there is no more zero-order focusing at infinite distance. These are the so called phase-reversal zone plates.

The theoretical ZP efficiency is achieved for opaque zones completely absorbing the incoming light or introducing a phase shift of π and transparent zones virtually 100% transparent for the incoming beam. The choice of both absorbing and transparent materials is therefore critical for achieving real ZP efficiency as close as possible to the theoretical one. In addition, absorption efficiency and phase shifting capabilities are also determined by the thickness t of the opaque zones, and therefore related to ZP fabrication strategies. As the lateral resolution of a ZP is inversely proportional to the width of the outermost zone, the best parameter that describes both resolution and efficiency of a ZP is the so called *aspect ratio*, defined as the ratio of outermost region thickness to its width.

For soft X-rays, ZP efficiency at first diffraction order approaches the theoretical value for a thickness of the optical element in the range of few hundreds of nanometers while the phase shift allows to further reduce the absorbing zone thickness [77]. Advances in e-beam lithography, reactive ion etching, electroplating techniques as well as in thin film technologies have guaranteed in recent years significant improvements both in resolution and in efficiency of FZP, allowing to overcome the 10 nm resolution limit for soft X-ray microscopy [78] and to produce structures with aspect ratios greater than 20:1 and an outer zone width of 25 nm [79]. For improving FZP efficiency for higher photon energies, thicker optical focusing elements have to be fabricated, therefore made by very high aspect ratio structures in order to preserve nanometer focusing. Sub-micrometer hard X-ray imaging can be routinely performed using ZP focusing elements, and several examples hard X-ray focusing down to 50 nm have been already published [80–82].

For improving both lateral resolution and efficiency of hard X-ray optics, Multilayer Laue lenses (MLLs) can be used. MLL is a one-dimensional ZP-like optic element [83] made of thousands of alternating layers fabricated by magnetron sputtering, the thickness of which obeys the zone plate law in the direction normal to the surface [84]. Magnetron sputtering is a thin-film deposition technique that enables the accurate deposition of a large number of alternating thin layers [85] and it allows overcoming the aspect ratio limitations in fabricating a ZP imposed by the conventional lithography methods. MLLs have been fabricated that produce 20 nm line focus with an efficiency of ∼30 % at 20 keV [86, 87]. Focusing capabilities below 1 nm have been postulated for MLLs [88] and outer zones having width down to 0.7 nm have been deposited by sputtering with an almost limitless aspect ratio [89]. In order to obtain a 2D focus, two MLLs focusing in orthogonal directions

have been recently assembled, similarly to KB mirrors [90]. Focusing capabilities to 25×40 nm FWHM spot with an efficiency of 17 % at 19.5 keV have been achieved, demonstrating the great potential of MLL optics for scientific applications.

References

1. L.G. Parratt, Phys. Rev. B **95**, 359–369 (1954)
2. W.H. Zachariasen, *Theory of X-ray Diffraction in Crystals* (Dover, New York, 1945)
3. J. Hrdý, Czech. J. Phys. B **39**, 261–265 (1989)
4. R. Frahm, Rev. Sci. Instrum. **60**, 2515–2518 (1989)
5. S. Narayanan, A.R. Sandy, M. Sprung, J. Sullivan, C. Preissner, D. Shu, AIP Conf. Proc. **879**, 911–914 (2007)
6. J. Als-Nielsen, G. Grübel, B.S. Clausen, Nucl. Inst. Methods Phys. Res. B **97**, 522–525 (1995)
7. E. Fonda, A. Rochet, M. Ribbens, L. Barthe, S. Belin, V. Briois, J. Synchrotron Rad. **19**, 417–424 (2012)
8. M. Lemonnier, R. Fourme, F. Rousseaux, R. Kahn, Nucl. Inst. Methods Phys. Res. A **152**, 109–111 (1977)
9. J.A. Golovchenko, R.A. Levesque, P.L. Cowan, Rev. Sci. Instr. **52**, 509–516 (1981)
10. D.M. Mills, M.T. King, Nucl. Inst. Methods Phys. Res. A **208**, 341–347 (1983)
11. J. Goulon, M. Lemonnier, R. Cortes, A. Retournard, D. Raoux, Nucl. Inst. Methods Phys. Res. A **208**, 625–630 (1983)
12. J.W.M. DuMond, Phys. Rev. **52**, 872–883 (1937)
13. G. Faigel, D.P. Siddons, J.B. Hastings, P.E. Haustein, J.R. Grover, J.P. Remeika, A.S. Cooper, Phys. Rev. Lett. **58**, 2699–2701 (1987)
14. H. Tolentino, A.R.D. Rodrigues, Rev. Sci. Instrum. **63**, 946–949 (1992)
15. K. Nakayama, H. Hashizume, A. Miyoshi, S. Kikuta, K. Kohra, Z. Naturforsch. Teil A **28**, 632–635 (1971)
16. S. Díaz-Moreno, J. Synchrotron Rad. **19**, 863–868 (2012)
17. T. Matsushita, T. Ishikawa, H. Oyanagi, Nucl. Inst. Methods Phys. Res. A **246**, 377–379 (1986)
18. H. Amenitsch, S. Bernstorff, M. Rappolt, H. Kriechbaum, H. Mio, P. Laggner, J. Synchrotron Rad. **5**, 506–508 (1998). See also www.elettra.eu/lightsources/elettra/elettra-beamlines/saxs.html
19. G. Aquilanti, O. Mathon, S. Pascarelli, J. Synchrotron Rad. **16**, 699–706 (2009)
20. F. Baudelet, Q. Kong, L. Nataf, J.D. Cafun, A. Congeduti, A. Monza, S. Chagnot, J.P. Itié, High Press. Res. **31**, 136–139 (2011)
21. www.elettra.eu/lightsources/elettra/elettra-beamlines/mcx.html
22. A. Di Cicco, G. Aquilanti, M. Minicucci, E. Principi, N. Novello, A. Cognigni, L. Olivi, J. Phys. Conf. Ser. **190**, 012043 (2009)
23. M. Born, E. Wolf, *Principles of Optics* (Pergamon Press, Oxford 1980)
24. M.C. Hutley, *Diffraction Grating* (Academic Press, London, 1982)
25. M.R. Howells, Section 4.3 in *X-Ray Data Booklet*, ed. by A.C. Thompson, D. Vaughan (Lawrence Berkeley National Laboratory, California, 2001)
26. E. Spiller, Chapter 12 in *Handbook on Synchrotron Radiation*, vol.1, ed. by E.E. Koch (North-Holland, Amsterdam, 1983), pp. 1093–1130
27. H. Haber, J. Opt. Soc. Am. **40**, 153–165 (1950)
28. P. Kirkpatrick, A.V. Baez, J. Opt. Soc. Am. **38**, 766–774 (1948)
29. W.B. Peatman, *Gratings, Mirrors and Slits—Beamline Design for Soft-X-ray Synchrotron Radiation Sources* (Gordon and Breach Science Publishers, Amsterdam, 1997)
30. H. Petersen, Opt. Commun. **40**, 402–406 (1982)
31. H. Petersen, SPIE **733**, 262–264 (1986)

32. W. Jark, Rev. Sci. Instrum. **63**, 1241–1246 (1992)
33. V.N. Strocov, T. Schmitt, U. Flechsig, T. Schmidt, A. Imhof, Q. Chen, J. Raabe, R. Betemps, D. Zimoch, J. Krempasky, X. Wang, M. Grioni, A. Piazzalunga, L. Patthey, J. Synchrotron Rad. **17**, 631–643 (2010)
34. www.elettra.eu/lightsources/elettra/elettra-beamlines/superesca.html
35. http://ssg.als.lbl.gov/ssgdirectory/arenholz/BL402.html
36. R. Follath, F. Senf, Nucl. Inst. Methods Phys. Res. A **390**, 388–394 (1997)
37. H. Petersen, C. Jung, C. Hellwig, W.B. Peatman, W. Gudat, Rev. Sci. Instr. **66**, 1–14 (1995)
38. R.L. Johnson, Chapter 3 in *Handbook on Synchrotron Radiation*, vol.1, ed. by E.E. Koch (NorthHolland, Amsterdam, 1983), pp. 173–260
39. C.T. Chen, F. Sette, Rev. Sci. Instrum. **60**, 1616 (1989)
40. R. Reininger, V. Saile, Nucl. Inst. Methods Phys. Res. A **288**, 343–345 (1990)
41. E. Dietz, W. Braun, A.M. Bradshaw, R.L. Johnson, Nucl. Inst. Methods Phys. Res. A **239**, 359–366 (1985)
42. R. Reininger, J. Bozek, Y. Chuang, M. Howells, N. Kelez, S. Prestemon, S. Marks, T. Warwick, C. Jozwiak, A. Lanzara, Hasan,M.Z., Hussain, Z. AIP Conf. Proc. **879**, 509–512 (2007)
43. H.A. Rowland, Philos. Mag. **13**, 469–474 (1882)
44. A. Rowland, Philos. Mag.**16**, 197–202 (1883)
45. L. Petaccia, P. Vilmercati, S. Gorovikov, M. Barnaba, A. Bianco, D. Cocco, C. Masciovecchio, A. Goldoni, Nucl. Inst. Methods Phys. Res. A **606**, 780–784 (2009). www.elettra.eu/lightsources/elettra/elettra-beamlines/badelph.html
46. www.elettra.eu/lightsources/elettra/elettra-beamlines/iuvs.html
47. http://www-ssrl.slac.stanford.edu/beamlines/bl5-4/
48. T. Kubala, M. Bissen, M. Severson, G. Rogers, D. Wallace, M. Thikim, M.V. Fisher, AIP Conf. Proc. **417**, 91–94 (2000)
49. http://www.src.wisc.edu/facility/list/Port_011.pdf
50. http://www.nsls.bnl.gov/beamlines/beamline.asp?blid=U13UB
51. T. Yamasaki, K. Yamazaki, A. Ino, M. Arita, H. Namatame, M. Taniguchi, A. Fujimori, Z.-X. Shen, M. Ishikado, S. Uchida, Phys. Rev. B **75**, 140513(R) (2007)
52. http://www.hsrc.hiroshima-u.ac.jp/
53. G. Reichardt, J. Bahrdt, J.-S. Schmidt, W. Gudat, A. Ehresmann, R. Müller-Albrecht, H. Molter, H. Schmoranzer, M. Martins, N. Schwentner, S. Sasaki, Nucl. Inst. Methods Phys. Res. A **467–468**, 462–465 (2001)
54. K. Radler, J. Berkowitz, J. Chem. Phys. **70**, 216–220 (1979)
55. P.A. Heimann, M. Koike, C.W. Hsu, D. Blank, X.M. Yang, A.G. Suits, Y.T. Lee, M. Evans, C.Y. Ng, C. Flaim, H.A. Padmore, Rev. Sci. Instrum. **68**, 1945–1951 (1997)
56. K. Ito, T. Sasaki, T. Namioka, K. Ueda, Y. Morioka, Nucl. Inst. Methods Phys. Res. A **246**, 290–293 (1986)
57. S. Hufner, *Photoelectron Spectroscopy* (Springer-Verlag, Berlin, 1995)
58. F. Reinert, S. Hufner, New, J. Phys. **7**, 97 (2005)
59. M.P. Seah, W.A. Dench, Surf. Interface Anal. **1**, 2–11 (1979)
60. B. Kaulich, P. Thibault, A. Gianoncelli, M. Kiskinova, J. Phys.: Condens. Matter **23**, 083002 (2011)
61. R. Falcone, C. Jacobsen, J. Kirz, S. Marchesini, D. Shapiro, J. Spence, Contemporary Physics **52**, 293–318 (2011)
62. A. Sakdinawat, D. Attwood, Nature Photonics 4, 840–848 (2010)
63. http://cheiron2007.spring8.or.jp/pdf/Lai.pdf
64. A. Snigirev, V. Kohn, I. Snigireva, B. Lengeler, Nature **384**, 49–51 (1996)
65. C.G. Schroer, J. Meyer, M. Kuhlmann, B. Benner, T.F. Günzler, B. Lengeler, C. Rau, T. Weitkamp, A. Snigirev, I. Snigireva, Appl. Phys. Lett. **81**, 1527–1529 (2002)
66. C.G. Schroer, M. Kuhlmann, U.T. Hunger, T.F. Günzler, O. Kurapova, S. Feste, F. Frehse, B. Lengeler, M. Drakopoulos, A. Somogyi, A.S. Simionovici, A. Snigirev, I. Snigireva, C. Schug, W.H. Schröder, Appl. Phys. Lett. **82**, 1485–1487 (2003)

67. C.G. Schroer, O. Kurapova, J. Patommel, P. Boye, J. Feldkamp, B. Lengeler, M. Burghammer, C. Riekel, L. Vincze, A. van der Hart, M. Küchler, Appl. Phys. Lett. **87**, 124103 (2005)
68. A. Bosak, I. Snigireva, K.S. Napolskii, A. Snigirev, Adv. Mater. **22**, 3256–3259 (2010)
69. E.L. Church, P.Z. Takacs, Opt. Eng. **34**, 353–360 (1995)
70. G.E. Ice, J.S. Chung, J. Tischler, A. Lunt, L. Assoufid, Rev. Sci. Instrum. **71**, 2635–2639 (2000)
71. K. Yamauchi, K. Yamamura, H. Mimura, Y. Sano, A. Saito, K. Endo, A. Souvorov, M. Yabashi, K. Tamasaku, T. Ishikawa, Y. Mori, Jpn. J. Appl. Phys. **42**, 7129–7134 (2003)
72. Y. Dabin, G. Rostaing, A. Rommeveaux, A.K. Freund, Proc. SPIE **4782**, 235–245 (2002)
73. C. Morawe, P. Pecci, J.C. Peffern, E. Ziegler, Rev. Sci. Instrum. **70**, 3227–3232 (1999)
74. S. Matsuyama, H. Mimura, H. Yumoto, Y. Sano, K. Yamamura, M. Yabashi, Y. Nishino, K. Tamasaku, T. Ishikawa, K. Yamauchi, Rev. Sci. Instrum. **77**, 103102–103106 (2006)
75. H. Mimura, S. Handa, T. Kimura, H. Yumoto, D. Yamakawa, H. Yokoyama, S. Matsuyama, K. Inagaki, K. Yamamura, Y. Sano, K. Tamasaku, Y. Nishino, M. Yabashi, T. Ishikawa, K. Yamauchi, Nat. Phys. **6**, 122–125 (2010)
76. M. Howells, C. Jacobsen, T. Warwick, A. van den Bos, in *Science of Microscopy*, ed. by P.W. Hawkes, J.C.H. Spence (Springer, New York, 2007), pp. 835–926
77. S.-R. Wu, Y. Hwu, G. Margaritondo, Materials **5**, 1752–1773 (2012)
78. J. Vila-Comamala, K. Jefimovs, J. Raabe, T. Pilvi, R.H. Fink, M. Senoner, A. Maassdorf, M. Ritala, C. David, Ultramicroscopy **109**, 1360–1364 (2009); W. Chao, J. Kim, S. Rekawa, P. Fischer, E.H. Anderson, Opt Express **17**, 17669–17677 (2009)
79. J. Vila-Comamala, S. Gorelick, V.A. Guzenko, E. Färm, M. Ritala, C. David, Nanotechnology **21**, 285305 (2010)
80. T. Koyama, H. Takano, S. Konishi, T. Tsuji, H. Takenaka, S. Ichimaru, T. Ohchi, Y. Kagoshima, Rev. Sci. Instrum. **83**, 013705 (2012)
81. G.C. Yin, Y.F. Song, M.T. Tang, F.R. Chen, K.S. Liang, F.W. Duewer, M. Feser, W.B. Yun, H.P.D. Shieh, Appl. Phys. Lett. **89**, 221122 (2006)
82. S. Gorelick, J. Vila-Comamala, V.A. Guzenko, R. Barrett, M. Salome, C.J. David, Synchrotron Radiat. **18**, 442–446 (2011)
83. H.C. Kang, J. Maser, G.B. Stephenson, C. Liu, R. Conley, A.T. Macrander, S. Vogt, Phys. Rev. Lett. **96**, 127401–127405 (2006)
84. C. Liu, R. Conley, A.T. MacRander, J. Maser, H.C. Kang, M.A. Zurbuchen, G.B. Stephenson, J. Appl. Phys. **98**, 113519 (2005)
85. H. Yan, Y.S. Chu, J. Synchrotron Rad. **20**, 89–97 (2013)
86. H.C. Kang, H.F. Yan, R.P. Winarski, M.V. Holt, J. Maser, C.A. Liu, R. Conley, S. Vogt, A.T. Macrander, G.B. Stephenson, Appl. Phys. Lett. **92**, 221114 (2008)
87. T. Koyama, H. Takenaka, S. Ichimaru, T. Ohchi, T. Tsuji, H. Takano, Y. Kagoshima, AIP Conf. Proc. **1365**, 24–27 (2011)
88. H.F. Yan, J. Maser, A. Macrander, Q. Shen, S. Vogt, G.B. Stephenson, H.C. Kang, Phys. Rev. B. **76**, 115438 (2007)
89. R. Conley, C. Liu, C.M. Kewish, A.T. Macrander, C. Morawe, Proc. SPIE **6705**, 670505 (2007)
90. H. Yan, V. Rose, D. Shu, E. Lima, H.C. Kang, R. Conley, C. Liu, N. Jahedi, A.T. Macrander, G.B. Stephenson, M. Holt, Y.S. Chu, M. Lu, J. Maser, Opt. Express **19**, 15069–15076 (2011)